Journal of Geochemical Exploration 204 (2019) 270–288

Contents lists available at ScienceDirect

Journal of Geochemical Exploration

journal homepage: www.elsevier.com/locate/gexplo

Distribution of REE-bearing minerals in felsic magmatic rocks and paleosols from Gran Canaria, Spain: Intraplate oceanic islands as a new example of potential, non-conventional sources of rare-earth elements

Inmaculada Menéndez[a,*], Marc Campeny[b,c], Luis Quevedo-González[a], José Mangas[a], Xavier Llovet[d], Esperança Tauler[c], Vidal Barrón[e], José Torrent[e], Jorge Méndez-Ramos[f]

[a] Instituto de Oceanografía y Cambio Global, IOCAG, Universidad de Las Palmas de Gran Canaria, 35214, Telde, Las Palmas de Gran Canaria, Spain
[b] Departament de Mineralogia, Museu de Ciències Naturals de Barcelona, 08003 Barcelona, Spain
[c] Departament de Mineralogia, Petrologia i Geologia Aplicada, Universitat de Barcelona, 08028 Barcelona, Spain
[d] Centres Científics i Tecnològics, Universitat de Barcelona, 08028 Barcelona, Spain
[e] Departamento de Agronomía, Universidad de Córdoba, Edificio C4, Campus de Rabanales, 14071 Córdoba, Spain
[f] Departamento de Física, Universidad de La Laguna, 38206 La Laguna, Tenerife, Spain

ARTICLE INFO

Keywords:
REE exploration
REE-bearing minerals
Weathering processes
Ocean intraplate volcanic island
Gran Canaria

ABSTRACT

Gran Canaria is a hotspot-derived, intraplate, oceanic island, comprising a variety of alkaline felsic magmatic rocks (i.e. phonolites, trachytes, rhyolites and syenites). These rocks are enriched in rare-earth elements (REE) in relation to the mean concentration in the Earth's crust and they are subsequently mobilised and redistributed in the soil profile. From a set of 57 samples of felsic rocks and 12 samples from three paleosol profiles, we assess the concentration and mobility of REE. In the saprolite that developed over the rhyolites, we identified REE-bearing minerals such as primary monazite-(Ce), as well as secondary phases associated with the edaphic weathering, such as rhabdophane-(Ce) and LREE oxides. The averaged concentration of REE in the alkaline bedrock varies from trachytes (449 mg kg^{-1}), to rhyolites (588 mg kg^{-1}) and to phonolites (1036 mg kg^{-1}). REE are slightly enriched in saprolites developed on trachyte (498 mg kg^{-1}), rhyolite (601 mg kg^{-1}) and phonolite (1171 mg kg^{-1}) bedrocks. However, B-horizons of paleosols from trachytes and phonolites showed REE depletion (436 and 994 mg kg^{-1}, respectively), whereas a marked enrichment was found in soils developed on rhyolites (1584 mg kg^{-1}). According to our results, REE resources on Gran Canaria are significant, especially in Miocene alkaline felsic magmatic rocks (declining stage) and their associated paleosols. We estimate a total material volume of approximately 1000 km^3 with REE concentrations of 672 ± 296 mg kg^{-1}, yttrium contents of 57 ± 30 mg kg^{-1}, and light and heavy REE ratios (LREE/HREE) of 17 ± 6. This mineralisation can be considered as bulk tonnage and low-grade ore REE deposits but it remains necessary to develop detailed mineral exploration on selected insular zones in the future, without undermining environmental and socioeconomic interests.

1. Introduction

According to the Union of Pure and Applied Chemistry (IUPAC), the elements in the REE group are Sc, Y and the 15 elements from the lanthanides group, i.e. La, Ce, Pr, Nd, Pm, Sm, Eu, Gd, Tb, Dy, Ho, Er, Tm, Yb and Lu (Connelly et al., 2005). REE are not as rare as the group name implies. The term “rare” is used because REE are very difficult to find in high enough concentrations for economic extraction. In the Earth's crust, the average concentration of REE ranges from 150 to 220 mg kg^{-1} (Rudnick and Gao, 2003), exceeding that of many other metals such as copper (55 mg kg^{-1}) and zinc (70 mg kg^{-1}), and they are intensely exploited by industrial mining (Long et al., 2010).

REE underpin a broad range of emerging technologies within state-of-the-art green energies, such as efficiency enhancement of solar cells and artificial photosynthesis, based on H_2 generation (Wondraczek et al., 2015). Indeed, REE occupy a very relevant position (holding the highest supply risk rate) in the list of Critical Raw Materials defined by the European Commission (2014), this includes REE and geological materials with a high economic relevance coupled with a high risk of supply.

* Corresponding author.
E-mail address: inmaculada.menendez@ulpgc.es (I. Menéndez).

https://doi.org/10.1016/j.gexplo.2019.06.007
Received 23 October 2018; Received in revised form 13 March 2019; Accepted 20 June 2019
Available online 24 June 2019
0375-6742/

The extreme supply risk of REE derives from the fact that China monopolises REE production worldwide (98% of global production in 2010 and around 85% at present) (Gambogi, 2017). Evidence of this is the global alarm in 2010, when the Chinese government drastically reduced export quotas, thus revealing the high vulnerability of the REE global market. Considering their critical economic role, the increasing demand for REE and the significant risks of supply, European governments promote exploration for new REE resources and the study of non-conventional geological environments including sedimentary rocks, soils and other weathering profiles (e.g. laterites and bauxites).

In the recent past, vertical distribution of trace REE was widely applied to control essential geochemical and weathering processes in soils, such as adsorption, solubility and transport factors (Tyler, 2004; Santana et al., 2015; Bern et al., 2017). In addition, the distribution of REE can also be used to determine the occurrence of Fe and Mn oxides in soils, due to the higher adsorptive affinity of LREE in the soil mineral lattice, compared to HREE (Chang et al., 2016).

However, several recent works carried out in different regions worldwide reported that REE contents in weathered rocks could also occur, not only at trace levels but also at concentrations of economic value. The first examples of economically significant REE contents in weathered rocks were reported in bauxites from China (Wang et al., 2000, 2003, 2010; Chai et al., 2001; Li et al., 2005) and, more recently, in Turkey, Greece (Deady et al., 2016) and in the Dominican Republic (Torró et al., 2017). Relevant REE concentrations have also been detected in laterites in regions such as Greece (Eliopoulos et al., 2014) and the Dominican Republic (Aiglsperger et al., 2016).

Paleosol REE-geochemistry has widely attracted scientific community interest. Studies have been carried out in worldwide locations, such as Southern China (Bao and Zhao, 2008; Wang et al., 2010; Chang et al., 2016), Brazil (Angelica and da Costa, 1991; Marques et al., 2004; Santana et al., 2015), Cameroon (Beyala et al., 2009), South Carolina (Foley and Ayuso, 2015), the Caribbean region (Aiglsperger et al., 2016; Torró et al., 2017), Cape Verde (Marques et al., 2004) and Spain (Fernández-Caliani, 2018; Reinhardt et al., 2018), among others. In all of these manuscripts, the study of the geochemical evolution of each area reflects the occurrence of weathering processes, the corresponding formation of soils and their relation with the concentration of metals (including Al and Fe but also minor elements, such as REE). It has also been noted how supergene products generate a significant variety of REE bearing minerals, such as aluminium-phosphate–sulphate (APS) phases (Dill et al., 1995) and phosphates, commonly monazite (Oelkers and Poitrasson, 2002; Marques et al., 2004; Santana et al., 2015).

Our investigation develops a geochemical exploration survey of the felsic, volcanic and associated sedimentary rocks from the three magmatic stages of the island of Gran Canaria. The first cycle corresponds to the Miocene-aged, alkaline declining stage, whereas the other two correspond to the Plio-Quaternary, volcanic rejuvenation stage. The study was focused on the REE distribution in the soils that developed on the alkaline felsic volcanic rocks from the island of Gran Canaria. The aim of the present study is to contribute towards the understanding of REE behaviour and accumulation in the soil profile and to evaluate the potential of soils developed from felsic volcanic rocks within intraplate oceanic islands as non-conventional sources of REE.

2. Geological setting

The island of Gran Canaria is approximately located at the centre of the Canary Islands archipelago (Fig. 1), which is a Cenozoic, hotspot-derived, intraplate system developed on oceanic Jurassic lithosphere (Schmincke, 1976, 1982; Hollik et al., 1991; Steiner et al., 1998). This island definition agrees with the Walker (1990) model of the intraplate oceanic islands formation, with submarine and subaerial stages. The island growth is similar to that described for other intraplate, oceanic, volcanic islands worldwide (Walker, 1990; Caroff et al., 1995; Le Dez et al., 1996; Carracedo et al., 2002; Hekinian et al., 2004; Schmincke and Sumita, 2010; Staudigel and Clague, 2010). The subaerial growth of Gran Canaria (Fig. 1) is characterised by a sequence of three main magmatic phases: the (i) shield-building, (ii) alkaline declining and (iii) volcanic rejuvenation stages, the last two were separated by an erosional gap of approximately 2 million years, between 7.3 and 5.3 Ma (Fuster et al., 1968; Lietz and Schmincke, 1975; McDougall and Schmincke, 1976; Feraud et al., 1981; Balcells et al., 1992; van den Bogaard and Schmincke, 1998; Schirnick et al., 1999; Guillou et al., 2004; van den Bogaard, 2013). The shield-building stage records the growth of a complex mafic shield between 14.5 and 14.1 Ma and the subsequent formation of a collapse caldera (Tejeda Caldera) at ca. 14.1 Ma (Schmincke and Swanson, 1966; Schmincke, 1982; Freundt and Schmincke, 1995) and highly explosive post-caldera volcanism (ca. 14.1 to 7.3 Ma). The volume of subaerial, mafic volcanic material erupted in the shield stage was about 1000 km^3 (Schmincke, 1976, 1982; Schmincke and Sumita, 2010). The Miocene mafic shield was overlaid with peralkaline, phonolitic-trachytic to rhyolitic lavas and ignimbrites (Fuster et al., 1968; Schmincke, 1976, 1990), intruded by a felsic cone-sheet swarm, dykes, domes and plugs (Schirnick et al., 1999). The estimated volume of subaerial, mafic and felsic volcanic material erupted at each stage totals about 1000 km^3 (Schmincke, 1976, 1982; Schmincke and Sumita, 2010). During the gap in volcanism, the island underwent strong erosion, which led to the formation of a radially arranged set of ravines and a large volume of sediment was deposited as alluvial and fan-delta conglomerates (fanglomerates), mainly on the S–SW and N–NE coastal platforms (Fuster et al., 1968; Lietz and Schmincke, 1975; Balcells et al., 1992). Rejuvenated volcanism comprised two main phases: (i) Roque Nublo, and (ii) Post-Roque Nublo (Fig. 1). The Roque Nublo phase (5.3 to 2.7 Ma (Guillou et al., 2004)) refers to the evolution of a complex stratovolcano in the central area of the island. The Roque Nublo stratovolcano emitted products with a basanitic and ankaramitic to trachytic and phonolitic composition, such as lava flows, ignimbrites and domes (Balcells et al., 1992; Pérez-Torrado et al., 1995). The volume of subaerial, mafic and felsic volcanic material erupted in this rejuvenation stage was about 200 km^3 (Schmincke, 1976, 1982; Schmincke and Sumita, 2010). The Post-Roque Nublo stage (3.7 Ma to present) is characterised by effusive and strombolian activity from vents aligned mainly along a NW–SE rift (Guillou et al., 2004). Firstly, mafic fissural volcanism (mostly lava flows and fall deposits) occurred with a progressive migration of emission centres to the north. Secondly, the so-called “platforming lavas” were randomly formed on the northern and eastern parts of the island, around 1.5 Ma. Finally, the most recent volcanism (< 1 Ma) involved the scattered strombolian and phreatomagmatic eruptions of alkaline, intermediate and mafic magmas over the central-northern part of the island. The volume of subaerial, mafic and intermediate volcanic material erupted during this rejuvenation stage was estimated to be 10 km^3 (Schmincke, 1976, 1982; Schmincke and Sumita, 2010).

3. Materials and methods

3.1. Sampling

This study was undertaken on a total of 57 samples of igneous bedrock, paleosol and sedimentary materials from Gran Canaria (Table 1a–1b and Fig. 1). In addition, 12 samples were selected from three representative paleosols, all of them from the Miocene alkaline declining stage: (i) the Fataga profile, developed on a trachy-phonolitic lava bedrock (R-PH; Figs. 2a, 3), (ii) El Queso profile, which comprised a trachy-rhyolitic ignimbrite bedrock (R-RH; Figs. 2b, 3), and (iii) the Culata profile, which is composed of trachytic lava bedrock (R-TR; Figs. 2c, 3). The Fataga profile (PH) consists of 20 to 30 cm of saprolite, a 20 to 30 cm weak red (10R5/3) B-horizon, a 30 to 50 cm very pale brown (10YR7/3) and a laminated B-horizon. The El Queso profile (RH) is formed by metric layers of weak, red rhyolitic ignimbrites (10R5/4) with saprolite, topped by a brown (7.5YR4/4) B-horizon. The Culata

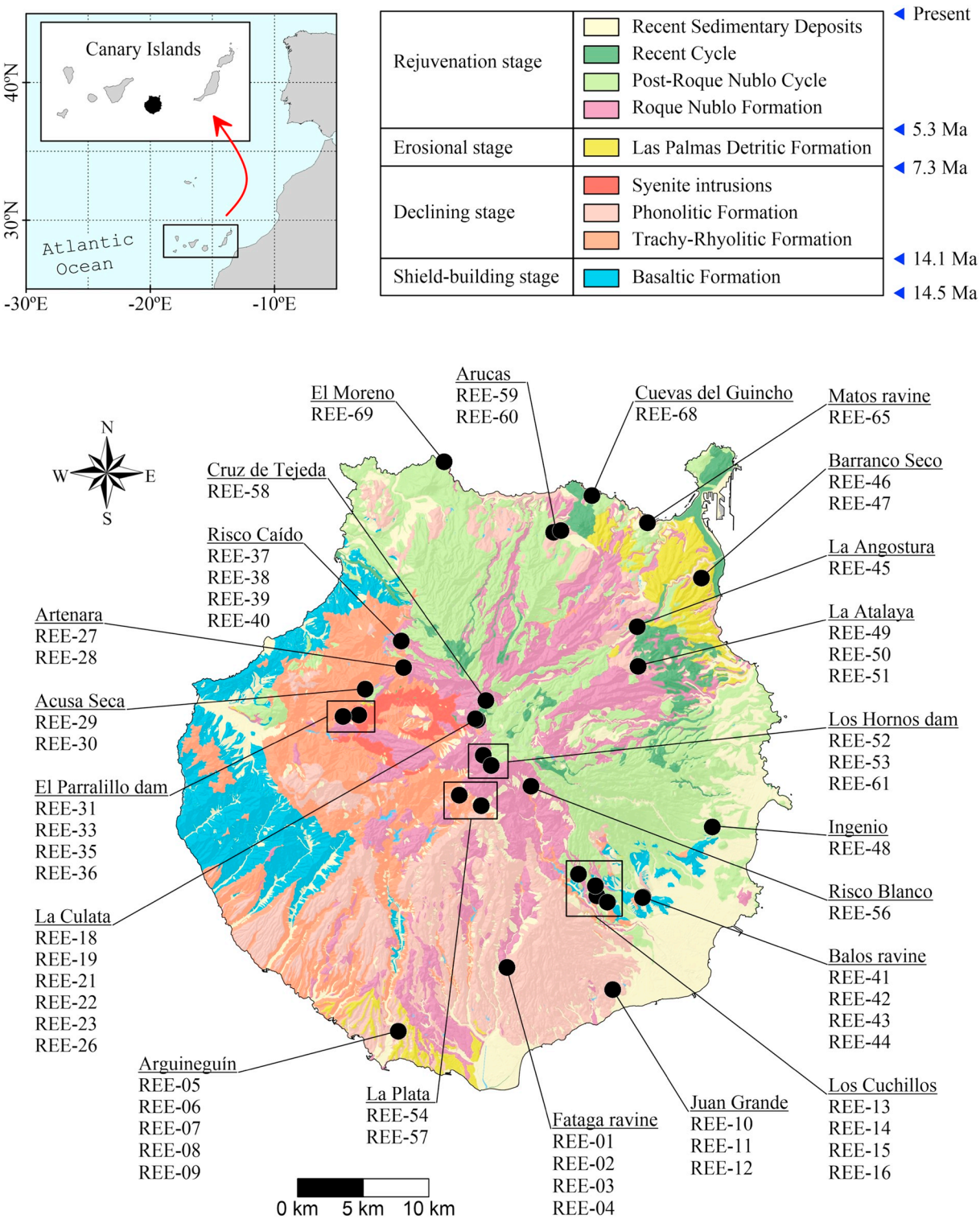

Fig. 1. Geographical setting (upper left), description of geological units (upper right) and geological map (main view) of Gran Canaria (modified after Bellido-Mulas and Pineda-Velasco, 2008). Sampling locations are also plotted (black dots). Sample names are shown in toponymical groups for clarity purposes.

profile (TR) is a well-developed and preserved profile consisting of two continuous saprolite levels, from 50 to 70 cm, at about 1 m depth, each being a reddish brown (5YR5/4) B-horizon and a, presumably truncated, 20 cm dark reddish grey (5YR4/2) BA-horizon.

3.2. Optical microscopy studies

Selected samples from each horizon profile were prepared as double-polished thin sections for their study under a petrographic microscope (Leitz Orthoplane), observed with both transmitted and reflected light. The microphotographs were taken with a Leica DFC 420 coupled camera. In addition, these thin sections were used for the microprobe analysis.

Table 1a
Sample set listed with geographical coordinates (WGS84; UTM zone 28 N), elevation (m asl) and location references for the igneous and sedimentary rocks collected within the Gran Canaria study area.

Sample	Easting	Northing	Elevation	Location
REE-01	443,025	3,077,367	472	GC-60 road, Degollada Las Yeguas
REE-02	443,025	3,077,367	472	GC-60 road, Degollada Las Yeguas
REE-03	443,025	3,077,367	472	GC-60 road, Degollada Las Yeguas
REE-04	443,025	3,077,367	472	GC-60 road, Degollada Las Yeguas
REE-05	434,771	3,072,482	91	Ceisa quarry, Arguineguín
REE-06	434,771	3,072,482	91	Ceisa quarry, Arguineguín
REE-07	434,771	3,072,482	91	Ceisa quarry, Arguineguín
REE-08	434,771	3,072,482	91	Ceisa quarry, Arguineguín
REE-09	434,771	3,072,482	91	Ceisa quarry, Arguineguín
REE-10	451,085	3,075,661	85	Lopesan quarry, Juan Grande
REE-11	451,085	3,075,661	85	Lopesan quarry, Juan Grande
REE-12	451,085	3,075,661	85	Lopesan quarry, Juan Grande
REE-13	449,878	3,082,826	550	GC-65 road, Los Cuchillos
REE-14	449,761	3,083,587	552	Montaña de las Carboneras, Los Cuchillos
REE-15	448,475	3,084,471	568	GC-550 road, Santa Lucía de Tirajana
REE-16	450,665	3,082,333	459	GC-65 road, Cuesta de Los Cuchillos
REE-18	440,783	3,096,230	1160	GC-608 road, La Culata
REE-19	440,783	3,096,230	1160	GC-608 road, La Culata
REE-21	440,783	3,096,230	1160	GC-608 road, La Culata
REE-22	440,783	3,096,230	1160	GC-608 road, La Culata
REE-23	440,783	3,096,230	1160	GC-608 road, La Culata
REE-26	440,641	3,096,312	1176	GC-608 road, La Culata
REE-27	435,157	3,100,231	1142	GC-210 road, Artenara
REE-28	435,157	3,100,231	1142	GC-210 road, Artenara
REE-29	432,247	3,098,579	810	GC-210 road, Acusa Seca
REE-30	432,247	3,098,579	810	GC-210 road, Acusa Seca
REE-31	431,765	3,096,604	514	GC-210 road, El Parralillo dam
REE-33	431,765	3,096,604	514	GC-210 road, El Parralillo dam
REE-35	430,559	3,096,485	315	GC-210 road, El Parralillo dam
REE-36	430,559	3,096,485	315	GC-210 road, El Parralillo dam
REE-37	434,982	3,102,241	931	Risco Caído, Artenara
REE-38	434,982	3,102,241	931	Risco Caído, Artenara
REE-39	434,982	3,102,241	931	Risco Caído, Artenara
REE − 40	434,982	3,102,241	931	Risco Caído, Artenara
REE-41	453,383	3,082,737	199	Los Corralillos, Balos ravine
REE-42	453,383	3,082,737	199	Los Corralillos, Balos ravine
REE-43	453,341	3,082,680	221	Los Corralillos, Balos ravine
REE-44	453,341	3,082,680	221	Los Corralillos, Balos ravine
REE-45	452,936	3,103,343	355	GC − 320 road, La Angostura
REE-46	457,838	3,107,038	93	GC-5 road, Barranco Seco
REE-47	457,838	3,107,038	93	GC-5 road, Barranco Seco
REE-48	458,648	3,088,079	176	GC-189 road, Ingenio
REE-49	452,975	3,100,322	555	La Atalaya parking, Santa Brígida
REE-50	452,975	3,100,322	555	La Atalaya parking, Santa Brígida
REE-51	453,018	3,100,318	548	La Atalaya quarry, Santa Brígida
REE-52	441,227	3,093,525	1609	GC-600 road, Los Hornos dam
REE-53	441,227	3,093,525	1609	GC-600 road, Los Hornos dam
REE-54	439,404	3,090,501	1226	La Lajilla quarry, GC-60 road, La Plata
REE-56	444,845	3,091,174	1031	GC-654 road, Risco Blanco
REE-57	441,068	3,089,684	1237	GC-60 road, La Plata
REE-58	441,433	3,097,709	1538	GC-150 road, Cruz de Tejeda
REE-59	446,588	3,110,526	334	Lomo Tomás de León, Arucas
REE-60	447,135	3,110,664	258	Lomo Tomás de León, Arucas
REE-61	441,830	3,092,760	1645	GC-600 road, Los Hornos dam
REE-65	453,717	3,111,267	34	Matos ravine, El Rincón
REE-68	449,505	3,113,343	85	GC-2 road, Cuevas del Guincho
REE-69	438,251	3,115,919	2	El Moreno headland, Gáldar

3.3. Powder X-ray diffraction (PXRD)

Samples of the selected profiles were crushed in an agate mortar, obtaining a particle size below 40 μm. The experimental profiles were performed using a PANalytical X'Pert PRO Alpha1 powder diffractometer at the Scientific and Technological Centre of the University of Barcelona (CCiTUB). The diffractometer equipment was used with monochromatised incident Cu Kα1 radiation at 45 kV and 40 mA and was equipped with a PS detector with an amplitude of 2.113°. The patterns were obtained by scanning random powders from 4° to 80° (2θ). Data sets were obtained by a scan time of 50 s at a step size of 0.017° (2θ) and a variable divergence slit. Mineral identification and semi-quantitative results were facilitated using the X'Pert search-match software with Powder Diffraction File, version 2 from JCPDS. When the occurrence of quartz was detected in the sample, it was used as an internal standard to correct diffraction patterns for instrumental shifts in the 2θ position. Quantitative mineral phase analyses were obtained by full refinement profile using TOPAS V4.2 software.

3.4. Scanning electron microscopy (SEM and FE-SEM)

A selection of these samples was examined on a scanning electron microscope (SEM) equipped with an energy-dispersive spectrometer (EDS), at the CCiTUB. The operating conditions were 15 to 20 kV accelerating voltage and 5 nA beam current. In addition, we carried out a more detailed study of REE mineral phases to determine their textural and qualitative compositional features with a JEOL JSM-7100 field emission scanning electron microscope (FE-SEM) at the CCiTUB.

3.5. Electron probe microanalysis (EPMA)

Further identification of REE mineral phases was started using EPMA spot analyses. EPMA was performed on a JEOL JXA-8230 electron microprobe with 5 wavelength-dispersive spectrometers (WDS) and a silicon-drift detector EDS, at the CCiTUB.

Three X-ray intensity maps of Ce, La, Fe, Al and P (plus backscattered electron images (BSE)) were collected using the EPMA operated in WDS mode by stage scanning, with an accelerating voltage of 20 kV and a beam current of 50 nA. The mapped areas were 92 × 92 μm, 280 × 420 μm and 112 × 140 μm, with dwell times of 10 ms, 50 ms and 40 ms per point, respectively. Pixel sizes (point spacing) were 0.18 μm, 0.70 μm and 0.28 μm, respectively. Spectrometers were peaked to the specific X-ray line positions using appropriate standards. Background maps, acquired with the WDS tuned to a background position on the right hand side of the corresponding peak, were subtracted from the corresponding peak intensity maps. Total map acquisition times were 2.0 h, 4.5 h and 7.0 h, respectively. Additional X-ray intensity maps for C, Al, Si, Cl, K, Ca, Ti, Mn and Ni were simultaneously collected in EDS mode.

Spot analyses were carried out with an accelerating voltage of 15 kV, a beam current of 10 nA and a focused beam, in order to achieve the best lateral resolution. Background positions were carefully adjusted. Analytical standards included natural and synthetic silicate, oxides and REE glasses as follows: apatite (Ca and P), UO_2 (U), ThO_2 (Th), LaB_6 (La), Ce_2O_3 (Ce), REE glasses (Pr, Nd), NiO (Ni), hematite (Fe), yttrium-aluminium garnet (Y), ZrO_2 (Zr), $Gd_3Ga_5O_{12}$ (Gd), and rhodonite (Mn). The correction procedure 'XPP' was used to convert specimen intensity ratios into concentrations. Counting times ranged from 20 to 40 s for both peak and background. Detection limits were ~300–400 mg kg^{-1} for Ca, P, Ni and Fe, ~500 mg kg^{-1} for Y, La and Ce, and ~1100–1300 mg kg^{-1} for U, Th, Pr, Gd and Nd.

3.6. Bulk rock geochemistry

Major, minor and trace element analyses of 57 samples of rock, sediment and paleosol were determined at the ACTLABS Activation Laboratories Ltd., Ontario (Canada). The major elements SiO_2, Al_2O_3, Fe_2O_3, TiO_2, K_2O, MgO, Na_2O, CaO, P_2O_5, MnO, Ba, Be, Sc, Sr, V, Y, and Zr were analysed by FUS-ICP, in addition to loss on ignition (LOI). Trace elements, including Ag, Bi, Cr, Cs, Co, Cu, Ga, Ge, Hf, In, Mo, Ni, Nb, Pb, Rb, REE, Sb, Sn, Ta, Th, Tl, U, W, Zn were analysed by FUS-MS; As, Au, Br, Hg, Ir, Sc, Se were analysed by INAA; Cd and S were analysed by TD-ICP. Major element detection limits ranged from 0.01 to 0.10 wt% (1 wt% equals 10,000 mg kg^{-1}) and trace element detection

Table 1b
Sample set sorted by island stage and geological formation, description of rock lithologies (V: volcanic; SV: subvolcanic; P: plutonic; S: sedimentary; VS: volcano-sedimentary) and bulk rock values of LREE (La—Eu), HREE (Gd—Lu), LREE/HREE ratios, total REE and yttrium (in mg kg^{-1}).

Stage	Formation	Sample	Type	Description	LREE	HREE	Σ REE	Y
Rejuvenation	Post-Roque Nublo	REE-48	VS	Red paleosol	397.46	31.71	429.17	43
(< 5.3 Ma)	(3.5 Ma - Present)	REE-58	VS	Red paleosol	583.97	32.29	616.26	35
		REE-68	V	Tephrite-phonolite lava flow	356.76	19.48	376.24	26
	Roque Nublo	REE-15	V	Trachytic lava flow	421.56	24.24	445.80	30
	(5.3–2.9 Ma)	REE-29	S	Sandstone	501.81	29.04	530.85	39
		REE-30	S	Siltstone	426.87	25.38	452.25	35
		REE-37	VS	Lahars	453.28	25.91	479.19	35
		REE-38	VS	Lahars	523.63	26.51	550.14	36
		REE-39	VS	Lahars	497.35	28.37	525.72	37
		REE-40	VS	Lahars	440.58	20.69	461.27	28
		REE-45	S	Paleosol	384.51	19.47	403.98	25
		REE-52	SV	Phonolitic collapsed dome	501.96	26.19	528.15	36
		REE-53	SV	Phonolitic edge dome	470.66	25.54	496.20	31
		REE-56	SV	Phonolitic dome	775.69	50.21	825.90	68
		REE-61	V	Block and ash ignimbrite	419.28	24.93	444.21	31
		REE-69	V	Block and ash ignimbrite	514.40	32.66	547.06	44
Erosional	Las Palmas Detritic	REE-46	S	Siltstone	382.10	23.04	405.14	26
(7.3–5.3 Ma)	Formation (LPDF)	REE-47	S	Siltstone	368.60	23.96	392.56	30
Declining	Trachy-phonolitic	REE-1	V	Phonolite lava flow	969.64	66.78	1036.42	102
(14.1–7.3 Ma)	(13.4–7.3 Ma)	REE-2	S	Paleosol	1082.03	89.29	1171.32	158
		REE-3	S	Paleosol	930.74	63.59	994.33	82
		REE-4	S	Paleosol	1053.29	85.68	1138.97	123
		REE-5	V	Ash and pumice ignimbrite	615.42	38.66	654.08	54
		REE-6	S	Paleosol	506.71	34.96	541.67	49
		REE-7	S	Paleosol	669.08	28.67	697.75	36
		REE-8	V	Ash and pumice ignimbrite	784.91	51.04	835.95	73
		REE-9	S	Paleosol	639.81	40.79	680.60	58
		REE-10	V	Phonolite lava flow	775.89	52.42	828.31	69
		REE-11	S	Paleosol	353.94	34.42	388.36	63
		REE-12	S	Paleosol	780.01	52.94	832.95	66
		REE-18	V	Ash and pumice ignimbrite	427.37	22.03	449.40	29
		REE-19	S	Paleosol	448.16	22.43	470.59	29
		REE-21	S	Paleosol	473.64	24.21	497.85	30
		REE-22	S	Paleosol	409.81	25.69	435.50	31
		REE-23	S	Paleosol	418.49	29.90	448.39	39
		REE-26	S	Paleosol	402.51	18.39	420.90	27
		REE-27	SV	Phonolitic dome	388.15	10.65	398.80	21
		REE-28	SV	Phonolitic dome top	322.02	10.53	332.55	20
		REE-31	SV	Phonolitic felsic dyke	718.76	38.21	756.97	60
		REE-33	SV	Trachytic felsic dyke	931.81	58.10	989.91	78
		REE-35	P	Intracaldera syenite	447.05	27.12	474.17	35
		REE-36	P	Intracaldera syenite	550.34	39.51	589.85	59
		REE-49	S	Paleosol	808.46	48.56	857.02	59
		REE-50	V	Ash and pumice ignimbrite	423.91	24.03	447.94	28
		REE-51	V	Ash and pumice ignimbrite	264.33	21.62	285.95	45
		REE-54	SV	Phonolitic dome	560.02	17.35	577.37	31
		REE-57	SV	Phonolitic dome	542.25	33.85	576.10	46
		REE-59	V	Block and ash ignimbrite	388.36	29.71	418.07	43
		REE-60	V	Block and ash ignimbrite	846.56	55.37	901.93	68
		REE-65	V	Block and ash ignimbrite	534.25	31.92	566.17	42
	Trachy-rhyolitic	REE-13	V	Rhyolitic lava flow	535.08	53.26	588.34	74
	(14.1–13.4 Ma)	REE-14	V	Block and ash ignimbrite	549.09	51.92	601.01	73
		REE-16	V	Ash and pumice ignimbrite	1484.10	100.05	1584.15	121
		REE-41	S	Siltstone base	1225.26	55.17	1280.43	74
		REE-42	S	Sandstone base	362.60	30.93	393.53	40
		REE-43	S	Siltstone roof	717.76	35.71	753.47	43
		REE-44	S	Sandstone roof	271.94	26.43	298.37	35

limits ranged from 0.01 to 1.00 mg kg^{-1}, except for gold (Au) in ppb, which had a detection limit of 1 μg kg^{-1}. Au, Hg and Ir concentrations are systematically below their respective detection limit for the used analytical methods.

Gains or losses of each element were measured as the percentage change of the elemental ratio between such elements in the weathering product and in the parent rock (Nesbitt, 1979) as follows:

$$\%\text{change of ratios} = 100\,[(Ri - Rp)/Rp] \quad (1)$$

Ri and Rp represent the element ratio in weathered samples and fresh bedrock respectively, assuming that volume does not change during weathering (Nahon and Merino, 1996). To compare the weathering degree of the profiles, we selected the Vogt's Residual Index (V), which is sensitive to subtle geochemical changes such as alteration at the water table and/or hydrothermal alteration along faults, using the molecular proportions as follows (Price and Velbel, 2003):

$$V = (Al_2O_3 + K_2O)/(MgO + CaO + Na_2O) \quad (2)$$

Moreover, the Chemical Index of Alteration (CIA) was calculated from the chemical analysis of the weathered materials and parent rocks, using the molecular proportions as follows (Nesbitt and Young, 1989; McLennan et al., 1993; Price and Velbel, 2003):

$$CIA = [Al_2O_3/(Al_2O_3 + K_2O + Na_2O + CaO)] \times 100 \quad (3)$$

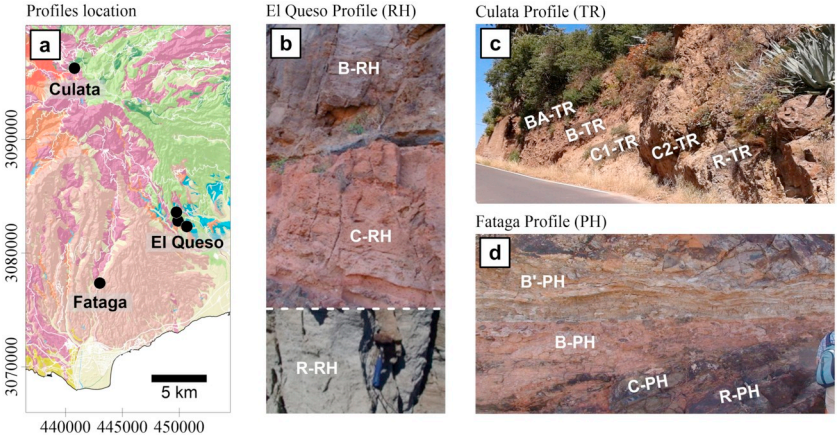

Fig. 2. (a) Geological map with the location of the studied samples (in black dots) and the respective name of the profiles, which are located in the south-eastern area of the island (see Fig. 1); (b, c, and d) Field photographs of El Queso, Culata and Fataga profiles with their related horizons (white labels). For more details, see Table 2a and 2b.

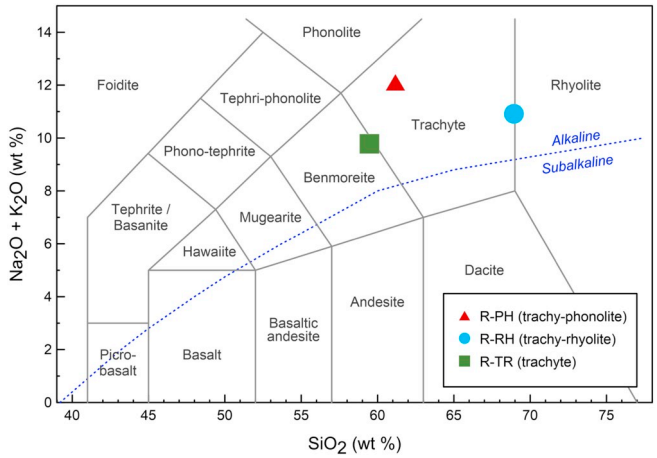

Fig. 3. TAS diagram for the volcanic bedrocks of the area studied (diagram after Le Bas et al., 1986; dashed curve from Irvine and Baragar, 1971).

Major element oxides are divided by their molar mass. The amount of CaO represents calcium in the silicate fraction. The TR and RH are carbonate free whereas, in the PH profile, the carbonate content is 1 to 3%. In the latter cases, CaOsilicate was calculated as (McLennan et al., 1993; Zhao et al., 2017):

$$CaO_{silicate} = CaO_{total} - (CaCO_3 \times 56.1/100.1) \quad (4)$$

3.7. Iron oxides: sequential extraction and diffuse reflectance analysis

Iron oxides of the RH profile, which presents the highest REE concentrations, were measured at the Department of Agronomy of the University of Córdoba. Three types of Fe oxides were sequentially extracted. Firstly, ferrihydrite (Fh), corresponding to the Fe dissolved with acid ammonium oxalate by the Schwertmann method (Schwertmann, 1964) (Fe_o); secondly, maghemite (Mgh), corresponding to the Fe extracted by sulphuric acid (Fe_s); and thirdly, the Fe in hematite (Hm) plus goethite (Gt), which were extracted using sodium dithionite in a hot (75 °C) sodium citrate and sodium bicarbonate solution (Mehra and Jackson, 1960) (Fe_d). If we assign Fe_d to the combination of Fe in stoichiometric Hm (α-Fe_2O_3) and Gt (α-FeOOH), the Gt content can be estimated as follows:

$$Gt = 1.59 \times (Fe_d - Hm/1.43) \quad (5)$$

The Hm/Gt ratio was estimated by means of diffuse reflectance spectroscopy (DRS; Scheinost et al., 1998; Torrent and Barrón, 2002; Torrent et al., 2007). The DRS is a precise and non-destructive method used to quantify soil properties and can detect the presence of either hematite or goethite at < 0.1% in mixtures with other soil minerals. The DRS spectra of the studied samples were recorded at a scan rate of 30 nm min^{-1} and from 380 to 770 nm in 0.5 nm steps, using a Varian Cary 5000 UV–Vis-NIR spectrophotometer equipped with a diffuse reflectance attachment. The relation between Hm and Gt was estimated from the amplitude of the Hm and Gt peaks of the second derivative spectrum of the Kubelka-Munk function (A_{Hm} and A_{Gt}), according to the equation given by Scheinost et al. (1998):

$$Hm/(Hm + Gt) = 0.068 + 1.325(A_{Hm}/(A_{Hm} + A_{Gt})) \quad (6)$$

Atomic Absorption Spectroscopy (AAS), using a Perkin-Elmer 420 instrument, was used to determine iron concentration in all extracts. The total Fe content (Fe_t), expressed as ion weight percentage, was calculated from the Fe_2O_3 weight percentage. REE concentration of the B-RH sample from the three extractions was measured by ICP after a digestion procedure, as described by Chang et al. (2016). The sample was mixed with 6 ml of concentrated HNO_3–$HClO_4$ (87:13, v/v) and 6 ml of concentrated HF (mass fraction 40%). The mixture was digested and then dissolved in 15 ml of 2% HCl solution.

4. Results

4.1. Mineralogy and textures

4.1.1. Bedrocks

The petrographic study of the trachy-phonolitic lava (Fataga profile, Fig. 2a) shows a fluidal trachytic texture, with microcryptocrystaline mesostasis surrounding the phenocrysts. The phenocrysts and microphenocrysts are mainly anorthoclase and, in minor amounts, nepheline, aegirine, kaersutite, biotite with oxidised rims, and haüyne. The mesostasis is composed of micro/crypto crystals of anorthoclase and, in minor proportions, nepheline, aegirine, kaersutite (occasionally with agpaitic texture), iron oxides, biotite, haüyne and clay minerals (Fig. 4a).

The trachy-rhyolitic block and ash ignimbrite (El Queso profile, Fig. 2b) present a tuffy texture of decimetric trachytic, syenitic and olivine-pyroxene basaltic rock fragments, devitrified pumice fragments, oligoclase and anorthoclase crystals and occasionally microcrystals of augite-aegirine, iron oxides, slightly weathered kaersutite, biotite, and devitrified cineritic mesostasis (Fig. 4b).

The trachytic ash and pumice ignimbrite (La Culata profile, Fig. 2c) presents a finely fragmented texture of ash, pumice, lithic and mineral fragments, typical of ignimbrite rocks (MacKenzie et al., 1984) with an irregular and discontinuous banding of felsic and ferromagnesian microcrystals, pumice and lithic fragments. This rock is formed of millimetric trachytic rock fragments, rare basaltic rock fragments, pumice fragments, anorthoclase millimetric crystals and, occasionally, microcrystals of iron oxides and biotite, as well as devitrified and

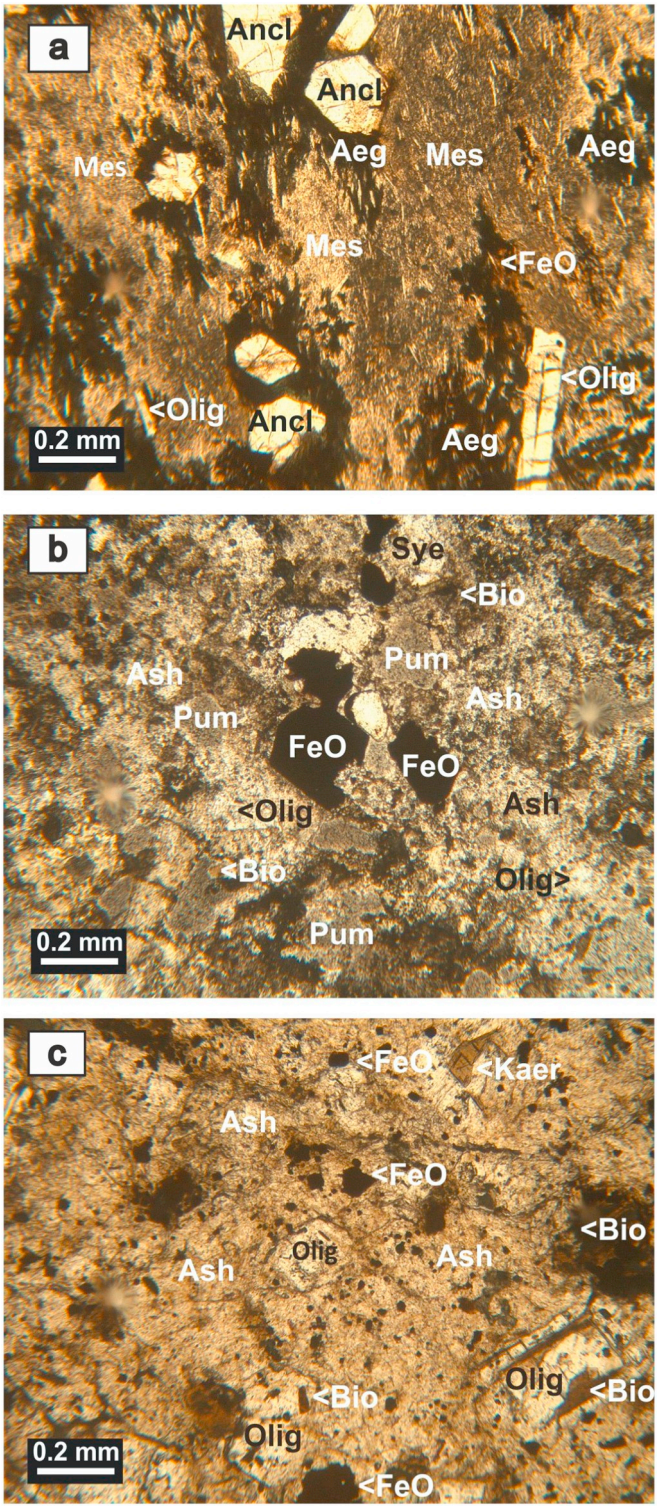

Fig. 4. Plane-polarised light microphotos (PPL, 40×) of Fataga (A, phonolitic lava flow), El Queso (B, block and ash ignimbrite) and Culata (C, ash and pumice ignimbrite) bedrocks. (Abbreviations - Ancl: anorthoclase; Aeg: aegirine; Olcl: oligoclase; Mes: mesostasis; FeO: iron oxides; Sye: syenite rock fragment; Bio: biotite; Pum: pumice; Kaer: kaersutite).

recrystallised cineritic mesostasis (Fig. 4c).

4.1.2. Paleosol horizons

The PXRD analysis of the paleosols horizons identified mainly anorthoclase and oligoclase with minor accessory phases (i.e. diopside,

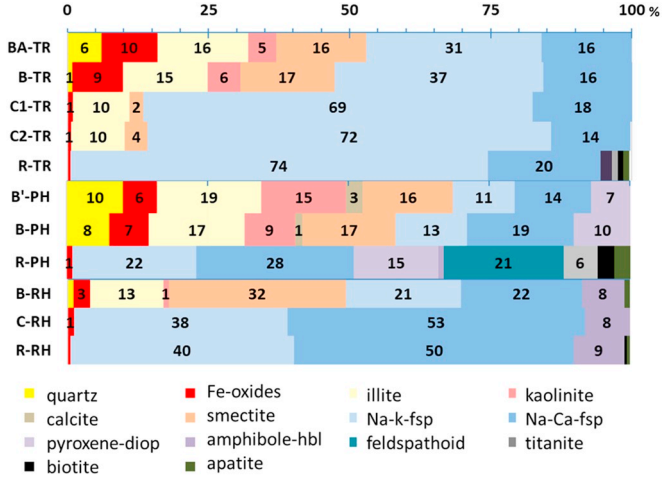

Fig. 5. Mineralogical composition of samples estimated by PXRD, except those for bedrocks by petrographic microscope analysis. X-axis refers to semi-quantitative mineral abundances expressed as rounded percentages. Y-axis legend: C, B, B′ and BA refer to soil horizons. PH: phonolite profile; RH: rhyolite profile; TR: trachyte profile.

hornblende, feldspatoids, titanite, biotite and fluorapatite). Weathering processes promoted depletion of the primary minerals and the formation of secondary phases, such as clay minerals (smectite, illite and kaolinite), calcium carbonates and iron and manganese oxyhydroxides. Also, we identified the occurrence of exotic quartz grains (Fig. 5) because the silica subsaturated nature of potential protoliths in the Canary Islands (Carracedo et al., 2002; Vera, 2004), precludes the occurrence of quartz in the volcanic paragenesis that built the islands.

The concentration of REE is conspicuously low and mainly concentrated in the upper part of the weathering profiles, in-filling the pores and small cavities and covering mineral surfaces (Fig. 6). These scarce REE minerals are mostly LREE-bearing phosphates that occur as euhedral to subhedral grains up to 10 μm in size (Fig. 7a-c).

Because of the small grain size and heterogeneity, accurate determination of the chemical composition of LREE-bearing phases is difficult. Reliable data were only obtained for a limited number of phases, such as monazite-Ce and rhabdophane-Ce. Representative EPMA analyses, along with the corresponding structural formulae of monazite-Ce and rhabdophane-Ce phases, are presented in Table 2. Fe—Mn and REE oxides were identified by SEM-EDS (semi-quantitative).

Monazite-(Ce) [(Ce,La,Nd)PO_4] is the most common REE phosphate and occurs as euhedral to subhedral isolated grains, exhibiting irregular borders. It is generally altered and presents light rims and lobate reaction fronts as described by Williams et al. (2011) for primarily altered domains (Fig. 7a). It also presents dissolution-precipitation textures where the monazite is transformed to rhabdophane-Ce (Fig. 7d-h). REE silicates (probably of the britholite group) have also been identified, associated with monazite-(Ce) and forming anhedral, subrounded grains up to 5 μm in size (Fig. 7d). Around these primary anhydrous phosphates, alteration halos often develop, made up of aggregated acicular crystals of rhabdophane-(Ce) [(Ce,La,Nd,Sm)$(PO_4)\cdot H_2O$] (Fig. 7d-f) and mostly accompanied by concentric layers of REE oxides (Fig. 7g-i).

4.2. Mineral chemistry of paleosols

In order to further examine the distribution of REE and their relation with other significant elements in the studied paleosol profiles, two background-corrected X-ray intensity maps, obtained on thin section from two different areas with previously detected occurrence of REE minerals, are presented in Figs. 8 and 9. A detailed inspection of the X-

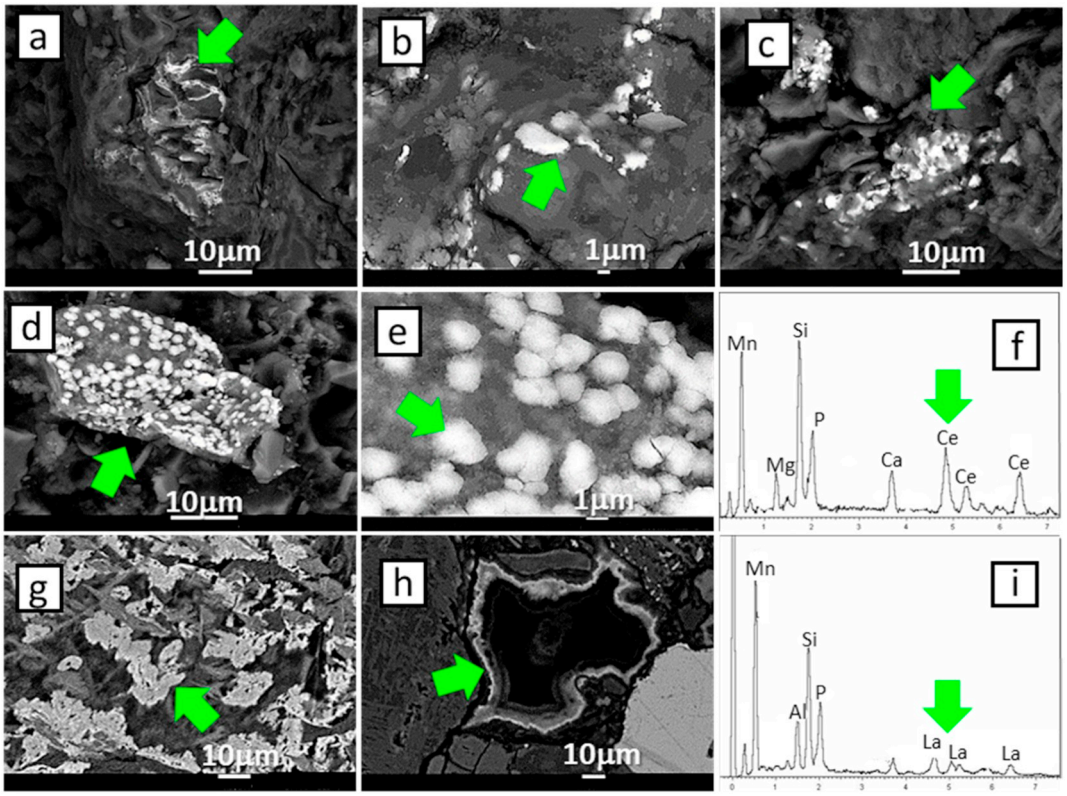

Fig. 6. SEM Backscattered-electron (BSE) images of REE bearing phosphates (green arrows) from a B-Horizon sample; (a-e) REE phases from the trachy-phonolite profile (PH); (f) semi-quantitative spectrum of REE phosphates identified from trachy-phonolite; (g-h) backscattering images from the trachy-rhyolite profile (PH); (i) semi-quantitative spectrum from trachy-rhyolite (RH). (For interpretation of the references to colour in this figure legend, the reader is referred to the web version of this article.)

ray maps showed the relationships between textural position, crystallisation sequence and mineral composition of the samples containing REE. Note that we acquired X-ray maps for several LREE (e.g. La, Ce, Py, Nd, Pm and Sm) but only La and Ce were detected and, consequently, are presented in Figs. 8-9. We also scanned for significant major elements related to the paleosol's mineralogy (i.e. C, Mg, Al, Si, P, Cl, K, Ca, Ti, Mn, Fe, and/or Ni).

The first map (Fig. 8) shows complex and variable textures. In general, the concentration of REE is mostly controlled by the occurrence of primary, isolated grains of LREE-rich phosphates, which were also detected during the previous mineralogical and textural studies using SEM and FE-SEM. The LREE-rich phosphates are mainly grains of monazite-(Ce) that may also contain significant amounts of La (Fig. 8, Table 2). We also found a second Ce-rich phosphate that forms thin concentric layers around the monazite-(Ce) grains (Fig. 9). This second phosphate does not contain La and it is associated with REE oxides and Mn oxyhydroxides (Fig. 8). Fig. 8 shows that the distribution of REE is mainly controlled by phosphate phases. REE contents are below detection limits or negligible in the silicates as well as in the carbonate phases present in the samples (Fig. 8).

In the second mapped area (Fig. 9), the distribution of REE shows similar features. Small isolated grains of Ce-rich phosphates, presumably identified as monazite-(Ce), are spread around the analysed area and control the distribution of LREE. However, in this case, the La contents are negligible (Fig. 9). Neither the carbonates nor the main silicates contain REE. The occurrence of Mn oxyhydroxides with very significant Ni contents are also highlighted (Fig. 9).

4.3. Bulk rock geochemistry

4.3.1. Major, minor and trace elements

The bedrock geochemistry of the major, minor and trace elements from the three profiles (Tables A-B in the Appendix A) show a depletion in MgO, Fe_2O_3 and CaO, an enrichment in silica (SiO_2), alkalis (K_2O and Na_2O) and Al_2O_3, and low concentrations of MnO, TiO_2 and P_2O_5 minor elements in relation to the first subaerial emissions (ultramafic, mafic and intermediate rocks). The concentration of trace elements is in agreement with this type of felsic rock, with low concentrations in compatible elements (Cr, Ni, Co, Sc, V) and an enrichment in incompatible elements (Rb, Sr, Ba, Nb, Zr and REE).

According to the TAS diagram (Fig. 3), the bedrocks are defined as trachytes, with slight differences: one is within the limit of the trachyte-benmoreite field (R-TR sample), another one is at the edge of the trachyte-phonolite field (R-PH sample) and the other is trachyte-rhyolite (R-RH sample). Consequently, these bedrocks are highly differentiated igneous rocks from the final stages of the fractional crystallisation.

4.3.2. REE

The REE concentrations in the bulk rocks from the first magmatic cycle of Gran Canaria, are similar to the associated felsic rocks of the Miocene alkaline declining stage and range between 532 ± 82 and 725 ± 196 mg kg^{-1} (Table 1b). Thus, the plutonic rocks (syenite stock) have a mean REE concentration of 532 ± 82 mg kg^{-1}; the subvolcanic rocks (trachy-phonolites dykes and domes) have a mean REE concentration of 725 ± 196 mg kg^{-1}; the volcanic rocks (trachy-phonolite and trachy-rhyolite lava flows and ignimbrites) have a mean REE concentration of 707 ± 340 mg kg^{-1}; the sedimentary rocks (sandstones and siltstone deposits) have a mean REE concentration of 681 ± 443 mg kg^{-1}; and the paleosols have a mean REE concentration of 684 ± 273 mg kg^{-1} (Table 1b). The mean REE concentration for alkaline declining stage is 672 ± 296 mg kg^{-1}, LREE/HREE ratio is 17 ± 5.8 and the mean yttrium (Y) concentration is 57 ± 30 mg kg^{-1}. The Miocene erosional stage was characterised by a lower REE concentration of 399 ± 8 mg kg^{-1} from the Las Palmas Detritic Formation

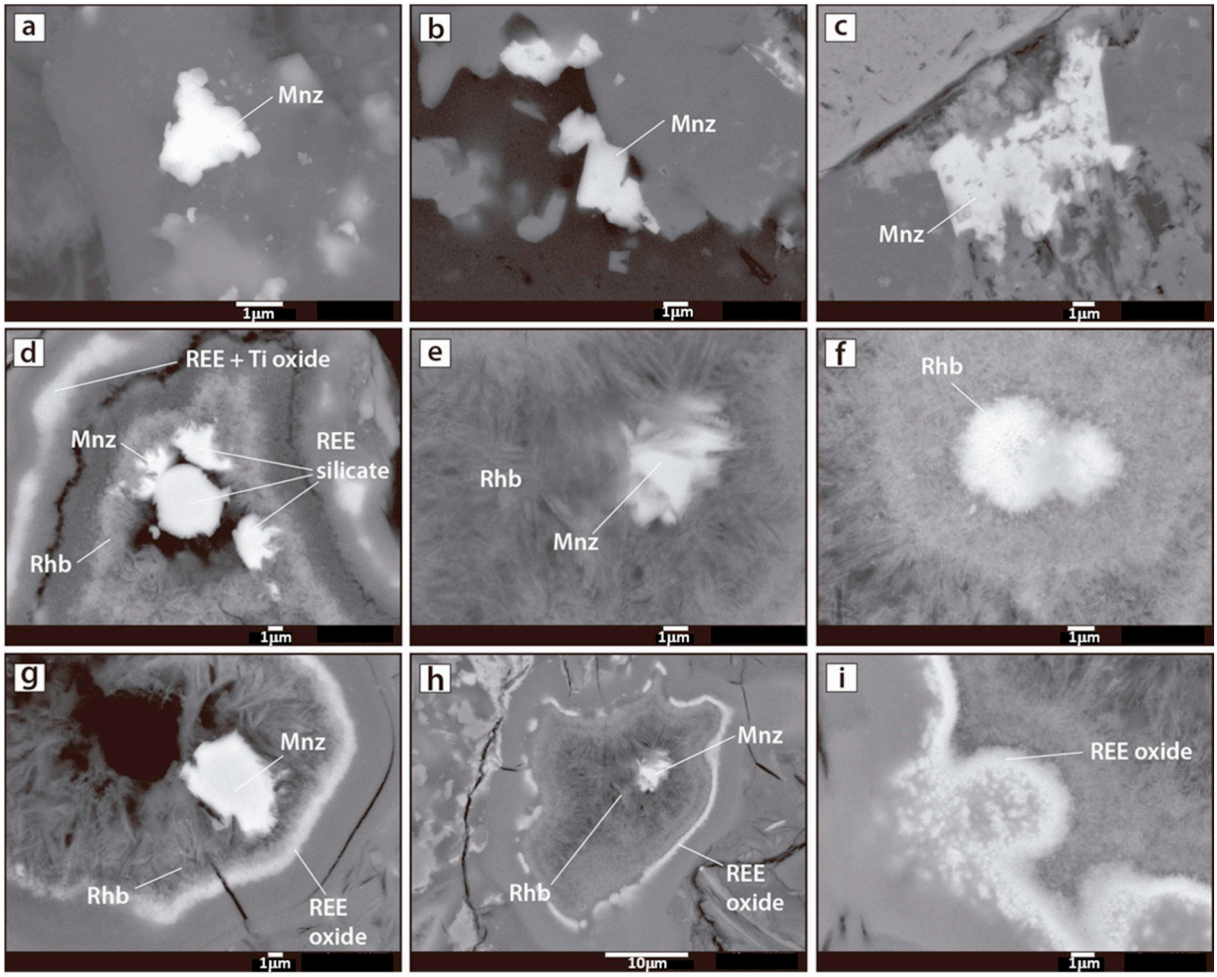

Fig. 7. FE-SEM Backscattered-electron (BSE) images of REE bearing minerals found in the upper parts of the studied weathering profiles from Gran Canaria; (a, b) individual monazite-Ce (Mnz) subhedral crystals with slightly rounded outlines; (c) monazite-Ce (Mnz) subhedral grain showing a sharp, irregular outline and abundant scratches; (d) anhedral grains of REE silicate accompanied by subhedral monazite-Ce (Mnz) crystals, surrounded by secondary fibrous rhabdophane-Ce (Rhb) and concentric REE oxides; (e) anhedral monazite-Ce (Mnz) grain floating in an alteration rim of fibrous rhabdophane-Ce (Rhb); (f) typical popcorn texture generated by foamy rhabdophane-Ce (Rhb) growing over a precursor monazite grain; (g, h) anhedral monazite-Ce (Mnz) grain embedded by fibrous rhabdophane-Ce (Rhb) surrounded by a concentric rim of REE oxides; (i) detail of a REE oxide concentric rim.

(siltstone). Chondrite-normalised plots showed a preferential concentration in LREE (Fig. 10).

The REE concentration of the second magmatic cycle (Roque Nublo Formation, with a magmatic total volume of 200 km^3), which was part of the rejuvenation stage of the island, presents a mean of 617 ± 182 mg kg^{-1} in the phonolitic domes; 563 ± 15 mg kg^{-1} in trachy-phonolitic lava flows and ignimbrites; 500 ± 41 mg kg^{-1} in epiclastic sedimentary rocks (sandstones and siltstone deposits); and a paleosol with a concentration of 404 mg kg^{-1}. These rocks, which are associated with the Pliocene magmatic chamber, show a REE concentration lower than the Miocene magmatic chamber.

The REE concentration of the third magmatic cycle (Post-Roque Nublo Formation, with an erupted volcanic rock volume of 10 km^3), is related to the rejuvenation stage of the island, and presents a value of 376 mg kg^{-1} for the tephrite-phonolite lava flow and a value of 523 ± 132 mg kg^{-1} for the two red paleosols. In this case, the REE concentrations are also lower than those of the Miocene magmatic chamber and the erupted felsic rocks are negligible in relation to the subaerial, insular vulcanism.

4.3.3. Element redistribution during soil formation

Geochemical losses and gains (% change of ratios) of the paleosol horizons with respect to the bedrock, differ between the three different profiles studied (Figs. 11-12, Tables C-D in the Appendix A). Mg, Ca, P, Fe, and Ti were highly retained in the RH paleosol profile but just maintained in the rest and even reduced in B-PH. Elements such as Mn and Al increased in the same proportions in all profiles, except for a reduction in B-PH. Silica, Na and K suffered a moderate reduction. Some elements such as Cr, Cu, Cs, Sr, Hf, Pb, Th, Sb, Sc, Be, REE, U, Nb, V, Y and Zn were concentrated in B-RH, except Hf (Fig. 12) but Sn Ge, Ga, Ba, Ta, Zr, Rb and Ag were depleted. However TR and PH profiles lost Pb and Sc and gained in Cr, Hf, Zn; Rb and V. Overall, the only ones that increased in concentration throughout all of the profiles were REE, Cr, Nb, Th, Y and Zn. V-index values increased upwards in a similar manner for the three profiles, being twofold in PH and TR with respect to RH. Likewise, the loss on ignition (LOI) values increased upwards in the profile, from parent rock to B-horizons (Table A in the Appendix A). The CIA index ranges from 48 to 52 in the bedrocks and 45 to 69 in the upper part of the profiles, with a generalised upwards increase, except for B-RH and BA-TR. The V index ranges from 0.4 to 1.7 in the bedrocks to 1.3 to 2.3 in the top horizons of the profiles, with a generalised increase upwards except for BA-TR (Table A in the Appendix A).

REE distributions were significantly modified during weathering (Fig. 13 and Table D in the Appendix A). An increase in REE concentrations was observed in all profiles. This increase was conspicuous for LREE in RH, whereas a slight decrease was also found for La in the

Table 2
EPMA analyses: composition of REE phosphates (monazite-Ce and rhabdophane-Ce) from Gran Canaria weathering profiles. (b.d.l. means below the detection limit).

Analysis N°.	Monazite			Rhabdophane		
	C-16	C-34	C-35	C-15	C-32	C-33
wt%						
FeO_t	0.30	1.73	3.49	1.36	0.30	1.45
CaO	0.71	0.57	0.17	1.03	0.86	0.96
P_2O_5	29.31	29.11	28.27	27.49	28.26	27.28
Y_2O_3	0.10	0.07	0.08	0.23	b.d.l.	0.24
ThO_2	b.d.l.	0.20	0.07	b.d.l.	0.27	0.15
UO_2	0.03	0.09	b.d.l.	b.d.l.	b.d.l.	0.15
La_2O_3	17.31	17.34	16.54	16.03	16.1	15.81
Ce_2O_3	35.34	34.48	35.34	32.54	33.79	33.02
Pr_2O_3	3.05	3.32	3.06	3.02	2.92	3.18
Nd_2O_3	11.13	10.67	11.83	10.19	10.6	10.81
H_2O				6.98	7.17	6.92
Total	97.27	97.58	98.85	91.89	93.09	93.05
apfu						
Fe_t	0.010	0.058	0.117	0.048	0.010	0.051
Ca	0.030	0.024	0.007	0.047	0.038	0.044
P	0.995	0.987	0.961	0.986	0.999	0.975
Y	0.002	0.001	0.002	0.005	b.d.l	0.005
Th	b.d.l	0.002	0.001	b.d.l	0.003	0.001
U	b.d.l	0.001	b.d.l	b.d.l	b.d.l	0.001
La	0.256	0.256	0.245	0.250	0.248	0.246
Ce	0.519	0.505	0.520	0.504	0.516	0.511
Pr	0.045	0.048	0.045	0.047	0.044	0.049
Nd	0.159	0.153	0.170	0.154	0.158	0.163
ΣREE	0.981	0.964	0.981	0.961	0.967	0.974

TR profile, and for Pr, Nd, Sm, and Tb in the upper part of B-PH. Chondrite-normalised plots showed a preferential concentration in LREE, both prominent in the PH and RH profiles (Fig. 14). None of the parent rocks show Ce anomalies but Eu differences were observed. Positive Ce anomalies were detected in the C and B-horizons of PH, C-horizon of RH and B-horizon of the TR profiles. An Eu negative anomaly remains in the PH profile and C-horizon in RH.

The Fe-Mn-P extractions performed for the trachy-rhyolite paleosol yielded a REE release efficiency of approximately 54% in Ce and about 17% for the rest of the REE when compared to the total amount of REE detected with total sample digestion (Fig. 15). The REE amount extracted from the poorly crystallised iron oxyhydroxides in soils (i.e. ferrihydrite and maghemite), ranged from 1.7 to 0.2% and from 1.4 to 6.3% respectively. For the more crystalline iron oxyhydroxides (i.e. goethite and hematite), REE extraction fluctuated from 92.6 to 98.4% of the total REE extraction.

5. Discussion

5.1. REE distribution

The redistribution of REE in weathered environments and soils may be controlled by different groups of phases, for instance, the aluminium-phosphate–sulphate (APS) minerals included in the alunite-jarosite group (Scott, 1987; Stoffregen and Alpers, 1987; Dill et al., 1995). However, all members of this group have been identified in the weathering profiles during the present work. A second mineral group that could also adsorb REE during weathering processes are clay minerals, as has been demonstrated by experimental studies (Coppin et al., 2002). Kaolinite may play an important role in removing REE from

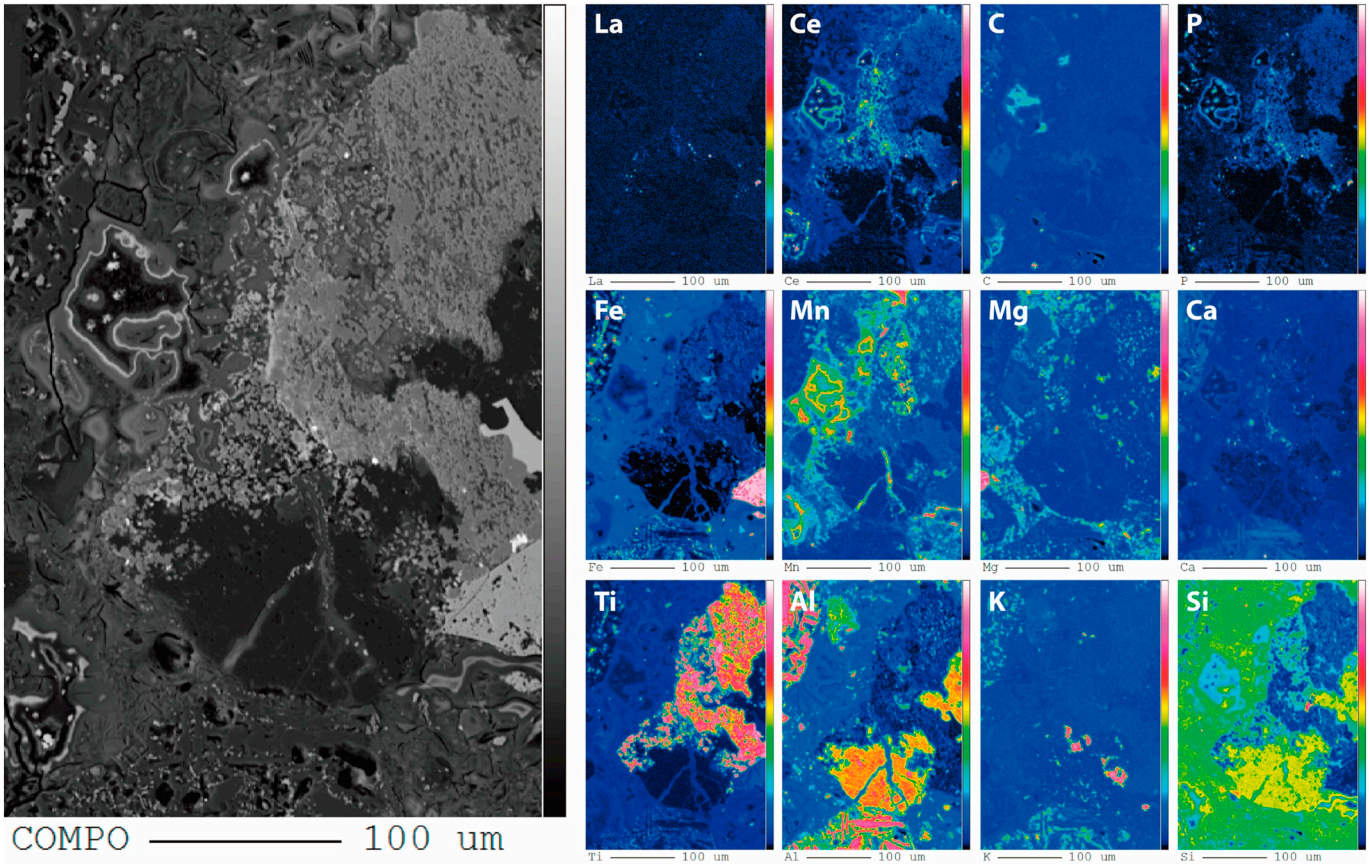

Fig. 8. Wavelength-dispersive X-ray maps of representative elements for B-RH sample.

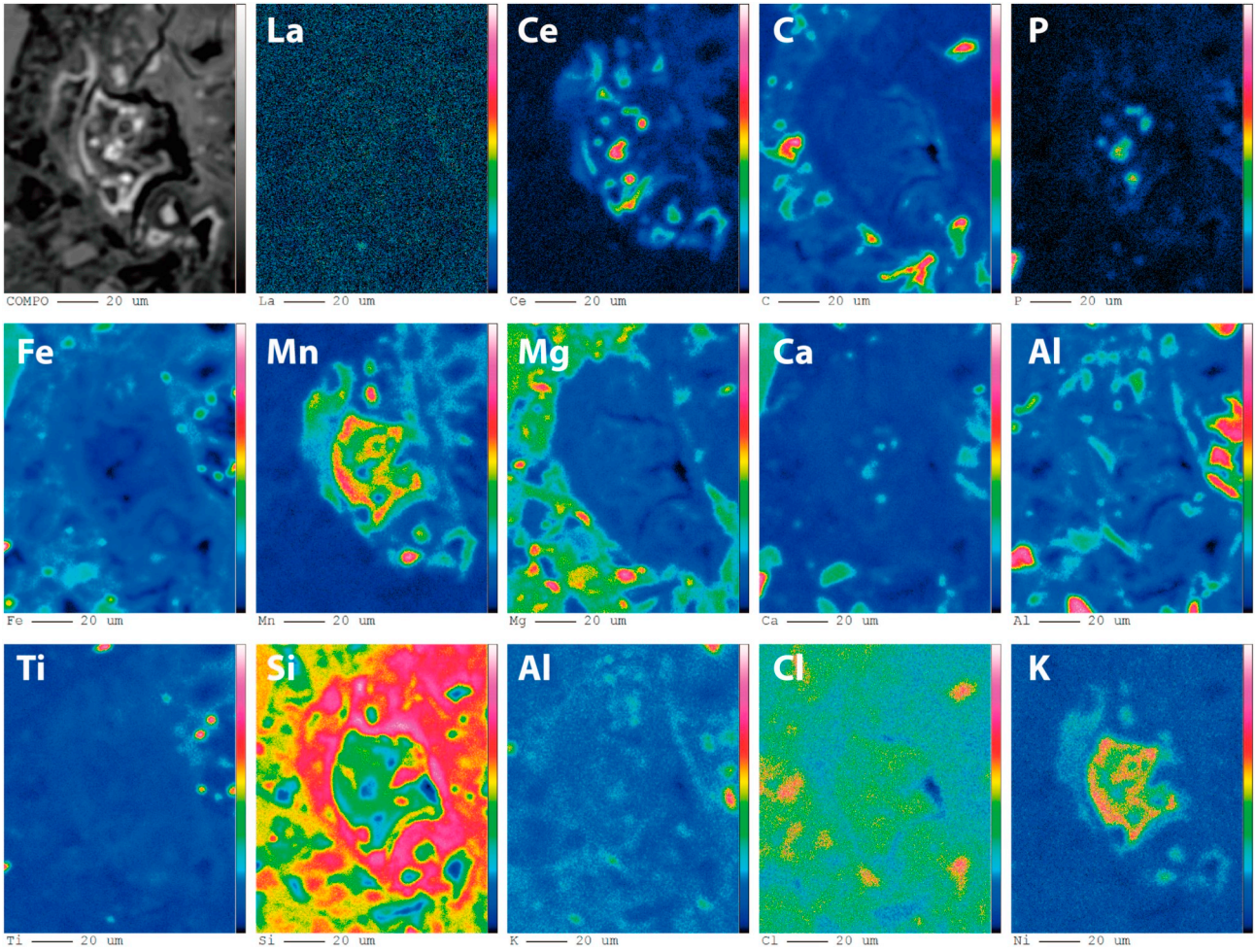

Fig. 9. Wavelength-dispersive X-ray maps of representative elements for B-RH sample. Target area is a void selected from Fig. 7.

aqueous solutions by sorption (Coppin et al., 2002; Karakaya, 2009). Conversely, Galán et al. (2007) found a lack of correlation between the total concentration of REE and kaolinite content in the clay-sized fraction. In the same way, relationships between kaolinite and REE were not found on our Gran Canaria profiles. We reported the existence of secondary illite, smectite and kaolinite generated by weathering but they present a clear lack of REE, as shown by the relation of Ce and Si compositional maps (Figs. 8 and 9). This suggests that adsorption onto the surfaces of clay minerals is probably not a prevailing mechanism of REE retention in the Gran Canaria profiles studied. Analogous results were observed in the laterite profiles developed on the Neogene basalts from the northern coast of Hainan Island, South China (Ma et al., 2007), where kaolin-group minerals did not present significant REE content.

The REE also present a high affinity for P-compounds (Tyler, 2004) and these REE-bearing minerals are very typical in weathered environments (Oelkers and Poitrasson, 2002; Marques et al., 2004; Santana et al., 2015). Indeed, on the basis of the mineralogical, textural and geochemical studies carried out in the present work, we can support such an affinity in the weathering profiles, where phosphates control the mineral distribution of REE (Fig. 6). Thus, we report monazite-(Ce) as a main REE phosphate (Fig. 7). This occurrence has been described in other paleosols and weathering profiles worldwide, such as the Las Mercedes bauxite deposit in the Dominican Republic (Torró et al., 2017), Greece bauxites (Eliopoulos et al., 2014) or the Quyang bauxites, China (Wang et al., 2010).

REE phosphate grains (monazite-(Ce)) show evidence for an authigenic origin: subhedral to anhedral crystals, irregular grain morphologies, rounded grain edges, oval to elongated grain shapes and partial dissolution at its borders (Fig. 7). We interpret that this REE phosphate is inherited from the bedrock and was not formed during weathering. However, weathering processes were able to generate the alteration of primary monazite-Ce and the corresponding mobilisation of REE, forming secondary phosphates during incipient stages of alteration (Zapata and Roy, 2004). In Gran Canaria soils, these secondary minerals are represented by rhabdophane-(Ce) which develops concentrically around primary crystals of monazite-(Ce), defining foamy aggregates that generate “popcorn” textures (Fig. 7f). This REE mineral association is similar to those reported in other localities worldwide (Braun et al., 1993; Taunton et al., 2000; Harlavan and Erel, 2002; Reinhardt et al., 2018). Lower alteration indexes (V and CIA-index) observed in the RH paleosol profile are evidence of slight weathering (Table 2a), coupled with the highest REE concentrations. In terms of weathering, CIA-indexes were lower in Gran Canaria profiles than in the other well-developed soils studied (Condie et al., 1995; Panahi et al., 2000; Galán et al., 2007; Bao and Zhao, 2008; Foley and Ayuso, 2013). As we previously suggested, Gran Canaria paleosols may not be strongly weathered. The occurrence of other secondary REE oxides developing concentric rims over inherited monazite-Ce and secondary rhabdophane-Ce (Fig.7 g-i) would be associated with significantly advanced stages of weathering (Table 4).

The existence of quartz in the upper layers of the paleosols (Fig. 5) has been related to an allochthonous provenance and can be used as a tracer of the aeolian inputs (Fernandez-Caldas et al., 1982; Mizota and Matsuhisa, 1995; Menéndez et al., 2007). In general, atmospheric deposition is a minor source of REE in soils (Wang et al., 2004) and it was confirmed on Gran Canaria in a previous study, in which current

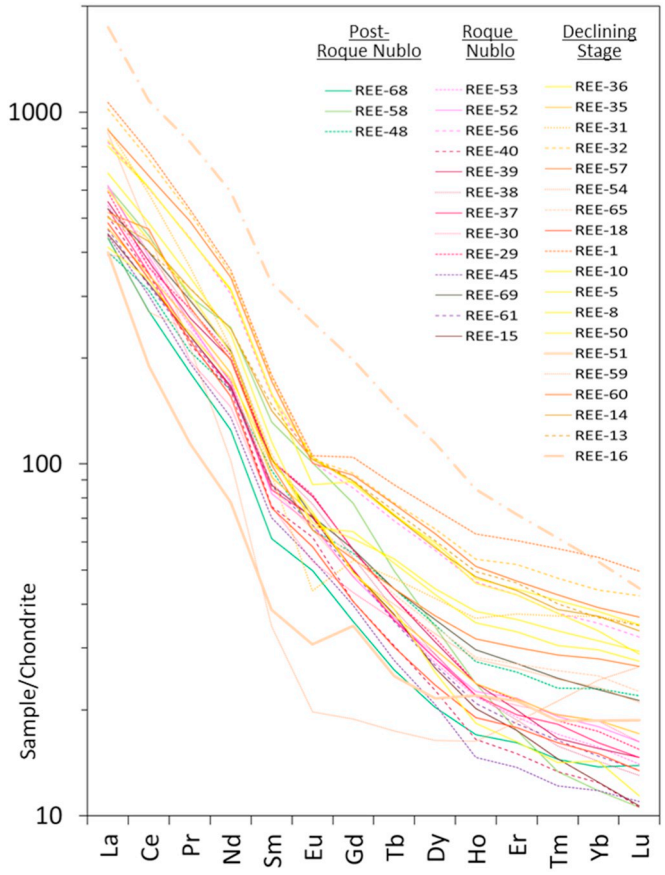

Fig. 10. Chondrite-normalised REE distributions of the samples from the different stages on Gran Canaria (sample code and description in Tables 1a–1b). Normalisation values after McDonough and Sun, 1995.

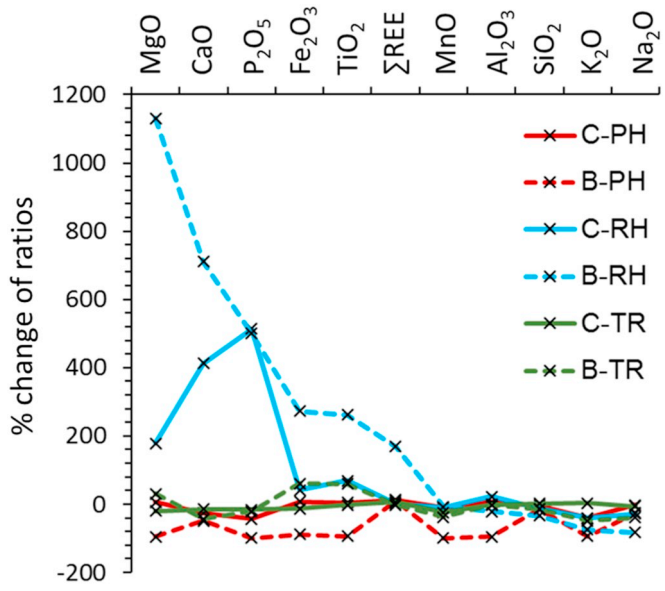

Fig. 11. Geochemical plots of relative losses and gains of major oxides from the studied profiles (% change of ratios, Eq. (1)) in paleosol horizons with respect to bedrock. REE totals are included for comparison. PH: phonolite profile; RH: rhyolite profile; TR: trachyte profile; C, B, B′ and BA refer to soil horizons.

aeolian dust deposits were analysed and showed lower REE concentrations than in the paleosol profiles (ΣREE = 226 mg kg^{-1}; Menéndez et al., 2019). Overall, the allochthonous components scarcely contribute to the REE bulk geochemistry of the upper soil horizons (Condie et al., 1995).

In soils, significant REE enrichment seems to be mostly associated with Mn oxides. There is numerous evidence of Ce enrichment in relation to Fe–Mn oxide formation (Ma et al., 2007; Tripathi and Rajamani, 2007; Feng et al., 2011). Frequently, the nano-sized REE oxides are below the spatial resolution of the spectroscopy tools, thus being difficult to observe (Yusoff et al., 2013). The association between LREE and Mn–Fe oxides suggests that Ce oxidation may have been performed through oxide-assisted scavenging of dissolved Ce(III) (Ohta and Kawabe, 2001; Ma et al., 2007; Pourret and Davranche, 2013; Yusoff et al., 2013). Since the incorporation of REE in the Fe–Mn-oxide structure is limited, sorption is one of the main mechanisms for REE scavenging onto Fe–Mn-oxides. Hence, REE contents are generally higher in amorphous Fe and Mn-oxides than in crystalline ones (Compton et al., 2003; Laveuf and Cornu, 2009). The REE tend to be higher in amorphous phases due to a possible expulsion during ageing and goethite crystallisation (Compton et al., 2003; Yusoff et al., 2013) or because the amorphous phase typically has a higher surface area for adsorbing ions. In the Gran Canaria profiles, the proportions of the poorly crystallised forms, ferrihydrite and maghemite, are significantly lower (8 to 24% of the total Fe concentration measured in C-RH and B-RH, respectively) than those of the crystallised phases of goethite and hematite (Fig. 15). Therefore, the bulk of the Fe-extractions of REE were mainly obtained from goethite and hematite forms (93 to 98% of the total REE measured in the Fe-extractions).

The presence of Fe oxides in paleosols suggests oxidising conditions. Thus, Ce is likely to be in the tetravalent state and, as a result, paleosols display a positive Ce anomaly in the trachyte and trachy-phonolite profiles (Table 2a and Fig. 15). According to Yusoff et al. (2013), the highest Ce(IV) concentrations are contained in cerianite and alumino-phosphates, localised in the pores in Mn-rich domains. In the C-horizon, Ce(III) and Ce(IV) are mainly distributed in REE-bearing minerals of the rhabdophane group, found in pores and cracks (Janots et al., 2006). In soils, Ce(III) oxidation into Ce(IV) is typically associated with the dissolution/precipitation processes that operate during weathering (Mongelli, 1997; Ma et al., 2007; Sanematsu et al., 2013; Yusoff et al., 2013).

Iron can co-precipitate with elements such as Al, Ti, Mn, Ni, Zn and Cr, among others, in the form of poorly crystalline phases, such as ferrihydrite (Cornell and Schwertmann, 2003, and references therein). In paleosols and very old soils, ferrihydrite has generally been transformed into hematite and/or goethite incorporating those elements. In addition, Gálvez et al. (1999) observed how phosphorus can be incorporated (or occluded) in the structure of the crystalline phases formed from the precursor ferrihydrite. Thus, in the studied profiles, the REE-bearing phosphates (rhabdophane- (Ce) and LREE oxides) might have co-precipitated with Mn and Fe oxides.

5.2. REE and weathering processes

The present study has revealed significant differences in REE concentrations when comparing the parent rocks (499 to 1036 mg kg^{-1}) with the corresponding weathering profiles (−42 to 0% change in the upper horizons and 2 to 169% in the lower ones). Even so, all lithologies present similar magnitudes in Ce (0.9 for negative anomalies and 1.1 to 1.3 for positive ones) and Eu anomalies (0.8 to 0.9 for negative anomalies and 1.1 for positive ones), as well as in LREE/HREE fractionation (from 16 to 33; Table 2a).

The increase of REE concentration during the weathering of the felsic volcanic rocks from Gran Canaria agrees with the results from other studies (Condie et al., 1995; Galán et al., 2007; Bao and Zhao, 2008; Yusoff et al., 2013; Calagari et al., 2015; Santana et al., 2015; Yanots et al., 2015). In contrast, depletion in REE during intense weathering of the parent rock has been reported by Beyala et al. (2009). There seems to be a preferential fixation of REE minerals in the early,

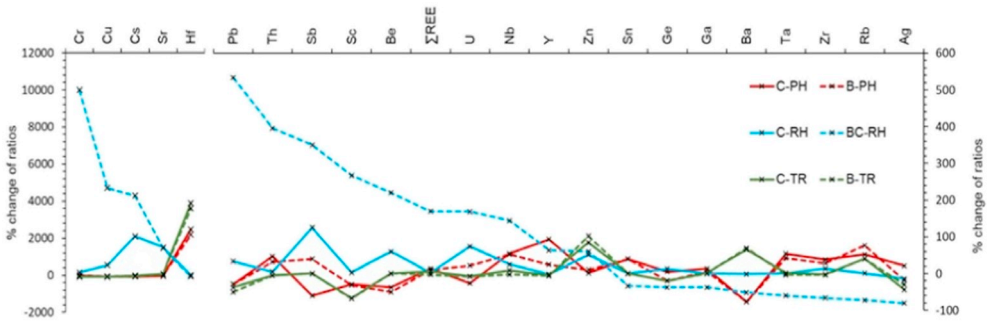

Fig. 12. Geochemical plots of relative losses and gains of trace elements from the studied profiles (% change of ratios, Eq. (1)) in paleosol horizons with respect to bedrock. REE totals are included for comparison. PH: phonolite profile; RH: rhyolite profile; TR: trachyte profile; C, B, B′ and BA refer to soil horizons.

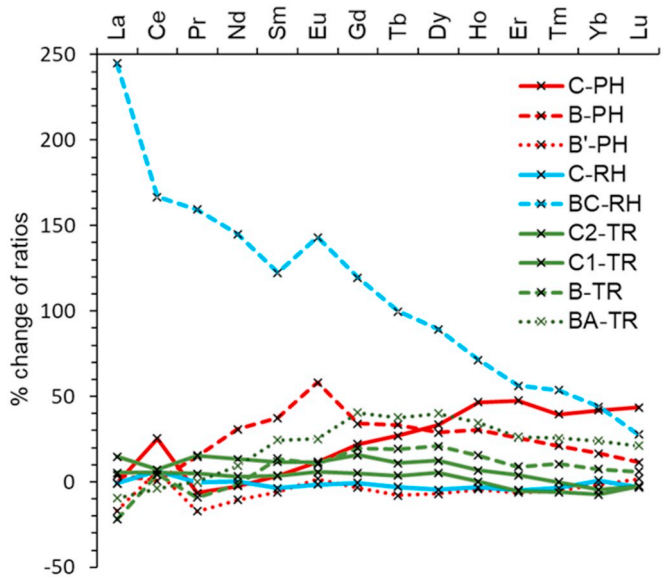

Fig. 13. Geochemical plots of the relative losses and gains of rare-earth elements from the studied profiles (% change of ratios, Eq. (1)) in paleosol horizons with respect to bedrock. PH: phonolite profile; RH: rhyolite profile; TR: trachyte profile; C, B, B′ and BA refer to soil horizons.

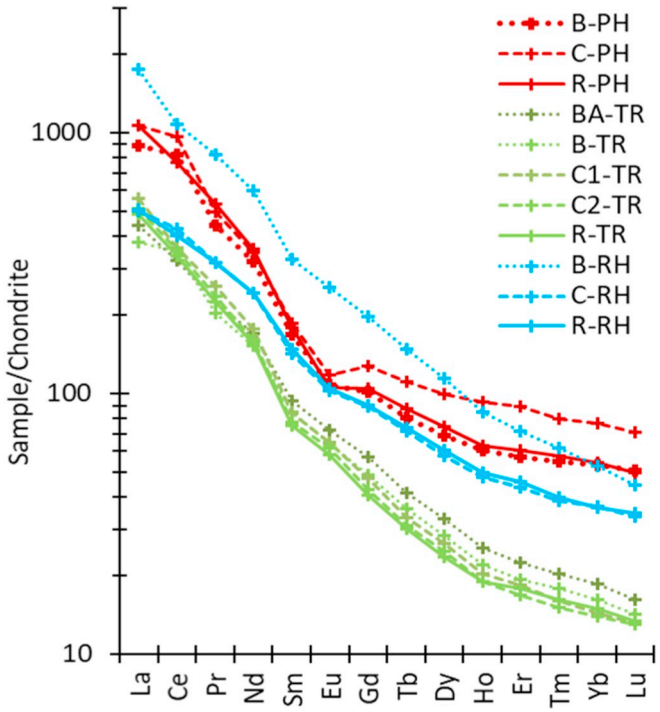

Fig. 14. Chondrite-normalised REE distributions of the samples from the selected profiles (normalisation values after McDonough and Sun, 1995). Legend: PH: phonolite profile; RH: rhyolite profile; TR: trachyte profile; C, B, B′, BA: soil horizons; R: bedrock.

rather than the more intense, weathering stages (Bao and Zhao, 2008). Primary mineral weathering occurs in all types of soils (Bockheim and Gennadiyev, 2000), thus dissolving accessory and essential phases (Nesbitt, 1979; Harlavan and Erel, 2002; Laveuf and Cornu, 2009). Moreover, an increase in REE concentration with depth has been described, a clear indication of leaching from the surface layers and deposition downward in the accumulation layers (Panahi et al., 2000; Ma et al., 2007; Chang et al., 2016). A variety of factors have been identified as influencing the retention of mobile REE, including preferential Mn (Ohta and Kawabe, 2001) and organic complexation (Taunton et al., 2000) and REE uptake by plant roots, linked to the absorption of Fe (Brioschi et al., 2013).

The REE mobilisation under supergene conditions involves the sequential release of REE and their redistribution along the weathering profile (Nesbitt, 1979). Europium and Cerium present two oxidation states at ground-surface conditions (Henderson, 1984; Laveuf and Cornu, 2009). The Ce^{+4} fixation on secondary minerals (Bao and Zhao, 2008; Laveuf and Cornu, 2009) might be the reason for the noticeable efficiency found in the dithionite extraction for Ce (54% of the Ce obtained by total digestion; Fig. 15). This result suggests that about 54% of this Ce could be absorbed by the Fe—Mn and LREE oxides (Figs. 4 to 7). Otherwise, it is necessary to remark that in the volcanic rocks, the REE are preferentially and randomly hosted within the vitreous mesostasis, thus hindering the REE-bearing mineral formation (Wilson, 1989). In addition, part of the Ce in the profiles still remains in cryptocrystallised form.

Under reducing conditions, Eu can be mobilised by phosphate and carbonate complexation (Wood, 1990). Negative Eu anomalies are, in most cases, related to the presence of feldspar or feldspar-derived alteration products, such as clay minerals (Galán et al., 2007).

Evidence for REE mobilisation in weathering profiles includes fractionation of LREE to HREE. However, this fractionation was primarily inherited from the felsic volcanic rocks (Fig. 14). The same pattern has been identified in rhyolitic dykes by Benaouda et al. (2017), where volcanism-related hydrothermal processes are held responsible for this fractionation. There is no evidence of general hydrothermalism in the Gran Canaria rocks and initial REE fractionation should be mainly inherited from magmatic REE fractionation. This fractionation continues through the weathering process, being enhanced in the upper part of the profiles (Table 2b) and absorbed by amorphous Mn and Fe oxides (Laveuf and Cornu, 2009; Beyala et al., 2009).

In the studied profiles, we consider immobile elements to be those that become concentrated during the mineral transformation processes,

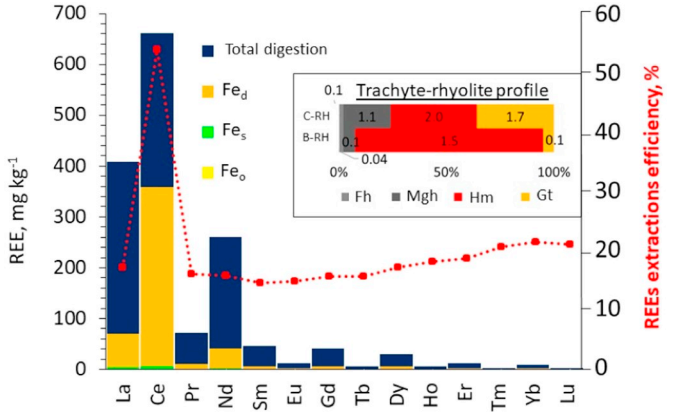

Fig. 15. REE concentration of the Fe–Mn extractions (bar plots, left axis) and REE extraction efficiency (dotted red line, right axis) for C-RH and B-RH samples from the El Queso profile. The inset graph (upper right) shows the proportions of the different Fe oxides determined for each sample. Total digestion refers to the total amount of iron oxides, dithionite extract (Fe_d) to hematite (Hm) plus goethite (Gt); sulphuric acid extract (Fe_s) to maghemite (Mgh), and acid ammonium oxalate extract (Fe_o) to ferrihydrite (Fh). (For interpretation of the references to colour in this figure legend, the reader is referred to the web version of this article.)

Table 4
Sequence of crystallisation for the REE-bearing mineral phases, depicting relationships between REE inherited phases (monazite-Ce), minerals generated during early stages of weathering (rhabdophane)-Ce, and LREE oxides associated with advanced stages of weathering. Note the close linkage between LREE oxides and Mn-oxyhydroxides.

mineral	formula	Inherited	Incipient weathering	Advanced weathering
monazite-(Ce)	$(Ce,La,Nd,Sm)PO_4$			
rhabdophane-(Ce)	$(Ce,La,Nd,Sm)(PO_4)\cdot H_2O$			
LREE oxides	$(Ce,La)O_2$			
Mn oxyhydroxides	$Mn(OH)_2$ / $Mn^{4+}O_2$			

despite their lack of mobility. Most of the elements are mobilised and transferred downwards through the weathering profile, as noticed in previous works (Ma et al., 2007). Nevertheless, TiO_2 and Zr are universally used for quantifying mass losses of major and trace elements in soils and other residual weathering products (Nesbitt, 1979; Brimhall and Dietrich, 1987). However, Bern et al. (2017) showed that Ti can be predominantly transported in the form of colloids. Other studies consider Th as an immobile element in tropical settings (e.g. Braun et al., 1993, 1998), but neither Th, TiO_2 nor Zr behave as immobile elements in the Gran Canaria profiles (Fig. 12). Physical weathering produces a loss of mass fragments, which leads to a preferential lixiviation of finer grain sizes. These processes subsequently involve a physical REE fractionation that is difficult to quantify. A positive percentage change should be detected for those elements but this trend depends on the profile (Figs. 11 to 13). Hence, none of the analysed elements appear to behave as if they were immobile (all positive values) except REE, Cr, Nb, Th, V, Y and Zn. Higher efficiency in their redistribution within the weathering profile probably implies that they were hosting the secondary minerals from the edaphic process. Secondary minerals (i.e. iron and manganese oxides) play an effective role in the transportation and concentration of a group of trace elements such as Co, Cr, and V, during weathering processes (Pokrovsky et al., 2006; Calagari et al., 2015). Rubidium is released during the break down of feldspar during weathering, thus explaining its depletion in RH but not in PH and TR paleosols.

The estimated weathering indexes (CIA and V-index, Table 2a) showed lower values in the RH profile, in concordance with REE decreasing with increasing degrees of weathering (Taunton et al., 2000; Chang et al., 2016), and in agreement with other studies of kaolinised profiles (Mongelli, 1993; Galán et al., 2007; Bao and Zhao, 2008; Yusoff et al., 2013). The CIA values of the upper parts of the profiles are lower than those obtained in other weathering profiles studied, for instance: CIA = 70 in Condie et al. (1995), CIA = 79 in Panahi et al. (2000), CIA = 91 in Galán et al. (2007), CIA = 98 in Bao and Zhao (2008), and CIA = 99 in Foley and Ayuso (2013). It is worth pointing out that our profiles are paleosols and are, therefore, always truncated. In any case, the CIA value of the most preserved profile (BA-horizon, TR) only reaches 63. Thus, we suggest that, despite truncation, the hereby reported weathering paleosol profiles from Gran Canaria were not fully developed.

Lastly, the results of Nesbitt (1979) and Duddy (1980) are particularly significant in showing that REE could just be redistributed, rather than lost, within a weathering profile. Net losses and/or gains of specific REE are not observed in the TH profile nor the PH profile, or in other studies, such as that by Condie et al. (1995). Further studies of the RH profile should be conducted in order to understand its substantial (threefold) increase in REE content.

5.3. REE mineralisation and environmental and socio-economic limitations for its exploitation on Gran Canaria

The occurrence of weathering and the corresponding formation of soils generated a significant enrichment of REE in these types of secondary formation, compared to the original primary rock (Angelica and da Costa, 1991; Foley and Ayuso, 2015). Therefore, secondary deposits should be considered as the most suitable targets when considering the potential exploration and corresponding exploitation of REE resources.

Gran Canaria is a limited territory (1560 km^2) with a population of 843,158 inhabitants, whose one major source of income is tourism (4.5 million tourists per year; ISTAC, 2017). The natural heritage (geodiversity and biodiversity) is valued and highly protected, mainly over the centre and south-western half of the island (49.4% of the island surface; source: Canary Government). In fact, both the local population and most of the services and facilities are concentrated in the north-eastern and eastern parts of the island and, hence, the proportion of protected areas here is much lower. Thus, most of the protected areas are concentrated in the south-west. The tourist industry is focussed along the southern and south-western coasts, where the Miocene mafic (shield phase) and felsic (decline phase) magmatic rocks from the first magmatic cycle mainly crop out. The few occurrences of Plio-quaternary magmatic rocks from the Roque Nublo and Post Roque Nublo Formations also crop out here, the latter being of minor interest to REE sources. Therefore, most of the key outcrops appear in protected areas, where extractive operations are prohibited and mining is not viable.

Our geochemical exploration study confirmed that the felsic magmatic rocks (phonolites, trachytes, rhyolites and syenites) and the associated paleosols of Gran Canaria can be considered to be a type of low-grade and bulk tonnage ore deposit for oceanic, intraplate volcanic islands, similar to that described by Jowitt et al. (2017) for highly fractionated rhyolites. The total volume of the felsic rocks in the alkaline declining stage (emitted between 14.1 and 7.3 Ma) is approximately 1000 km^{-3} (Schmincke, 1976, 1982; Schmincke and Sumita, 2010) and, assuming that these rocks have a density of 2700 kg m^{-3}, this yields 2700 MT. Taking into account the mean 672 mg kg^{-1} REE grade in this alkaline stage, the total tonnage of REE on Gran Canaria would be about 1814 MT of potential REE resources. Accordingly, intraplate oceanic islands with alkaline felsic rocks (lava flows, ignimbrites and plutonic stocks) can be considered as new potential, non-conventional rare-earth element resources.

Nevertheless, the gross amount of about 1.814 MT of potential REE resources must be recalculated downwards due to the limitations of the area occupied by the protected natural spaces, the dispersed rural population and the numerous coastal tourist infrastructure. For all these reasons, it would be necessary to carry out a detailed geochemical

exploration in outcrops of felsic rocks and paleosols that are free of these environmental and socio-economic conditions.

The results obtained within this study, comprising the geochemical exploration of REE on this hotspot-derived volcanic island, can serve as a guide for future mineral prospects in these oceanic, intraplate environments. The felsic magmatic rocks related to the insular alkaline declining stage, which appear after the shield-building stages in all hotspot archipelagos, are the most suitable materials in which to carry out mineral exploration for REE. However, since islands are small geological features, mostly constrained by both environmental and socioeconomic issues, the potential exploitation of these resources might be restricted.

6. Conclusions

Bulk major and trace geochemistry has been analysed in a set of felsic magmatic rocks and related paleosol profiles from different magmatic episodes on the island of Gran Canaria. A substantial mobilisation of REE, among other elements, has taken place during the course of the soil-forming processes. Our key findings can be summarised as follows:

(i) REE concentrations are significantly relevant in these types of differentiated magmatic materials, in terms of the estimated volume erupted during the alkaline declining stage of the island of Gran Canaria (1000 km^3 over 7 Ma), which averages a REE sum of 672 ± 296 mg kg^{-1}, an yttrium content of 57 ± 30 mg kg^{-1}, and a LREE/HREE ratio of 17 ± 6;
(ii) REE concentrations vary from 2 to 169% in the lower horizons and are associated with phosphates (such as primary monazite-(Ce)), and with secondary soil weathering products linked to the co-precipitation of Fe−Mn oxides (such as rhabdophane-(Ce) and LREE oxides), but not to clay minerals, such as smectite, kaolinite or illite;
(iii) High LREE/HREE fractionation and slightly negative Eu anomalies were mainly inherited from the parent rocks, whereas positive Ce anomalies were enhanced by soil development;
(iv) REE were found to be evenly redistributed in newly-formed minerals (i.e. rhabdophane-(Ce) and LREE oxides), particularly in the case of cerium, mainly linked to crystalline oxides, such as goethite and hematite, rather than to amorphous phases.

As a corollary, on the basis of our results, this research supports the potential of felsic materials derived from the declining stage of an oceanic intraplate volcanic island, such as Gran Canaria, as being a type of low-grade and bulk tonnage REE ore deposit. However, environmental and socioeconomic factors may drastically limit the extension of island-based, REE-enriched deposits in terms of long-term exploitation.

Declaration of Competing Interest

No potential conflict of interest was reported by the authors

Acknowledgments

This work presents part of the research results arising from the projects: *Materials for advanced power generation* (ENE2013-47826-C4-4-R) and, *3D Printed Advanced Materials for Energy Applications* (ENE2016-74889-C4-2-R), both funded by the Government of Spain. We thank the anonymous reviewers for their helpful comments that have improved the clarity and quality of the manuscript. This research did not receive any specific grant from funding agencies in the public, commercial, or not-for-profit sectors. Hereby, we want to dedicate this paper to the principal researcher of these projects, PhD Juan Carlos Ruiz Morales who passed away too young.

Appendix A

Table A
Major and rare-earth elements geochemistry of samples from the selected weathering profiles (major oxides in wt%, REE in mg kg^{-1}). Geochemical composition of the samples from the selected weathering profiles.

Profile	Fataga				El Queso			Culata				
Lithology	trachy-phonolite				trachy-rhyolite			trachyte				
Sample	REE-01	REE-02	REE-03	REE-04	REE-13	REE-14	REE-16	REE-18	REE-19	REE-21	REE-22	REE-23
Horizon	R-PH	C-PH	B-PH	B′-PH	R-RH	C-RH	B-RH	R-TR	C2-TR	C1-TR	B-TR	BA-TR
SiO2	58	56	48	49	68	59	45	56	58	58	48	49
Al2O3	16	17	20	18	14	17	11	18	18	18	18	17
Fe2O3	6	6	6	7	4	6	15	6	5	5	9	10
MnO	0.5	0.4	0.3	0.4	0.2	0.2	0.3	0.1	0.1	0.2	0.1	0.1
MgO	1.2	1.2	1.2	1.6	0.5	1.5	6.5	0.9	0.7	0.8	1.2	1.3
CaO	1.2	0.9	3.0	2.1	0.5	2.8	4.4	2.3	2.1	1.8	1.3	1.5
Na2O	6.8	4.0	1.3	1.9	7.0	4.2	1.8	4.5	4.9	4.5	2.3	2.4
K2O	4.7	4.8	2.3	2.5	3.8	2.8	0.6	4.8	4.4	4.5	2.9	3.2
TiO2	1.0	1.1	1.0	1.2	0.8	1.3	2.8	1.5	1.6	1.5	2.5	3.0
P2O5	0.1	0.0	0.0	0.1	0.1	0.3	0.3	0.3	0.4	0.2	0.3	0.4
LOI	4	8	15	16	1	5	12	4	4	5	13	10
Total	99	99	99	100	100	100	99	99	99	99	99	99
La	253	251	210	263	120	119	414	115	121	132	90	104
Ce	472	592	503	475	247	263	659	206	217	221	215	198
Pr	49	46	41	57	29	29	76	21	22	24	19	21
Nd	163	159	146	213	111	111	272	71	73	81	70	78
Sm	27	27	25	36	22	21	49	11	12	12	13	14
Eu	6	7	6	9	6	6	14	3	3	4	4	4
Gd	21	25	20	28	18	18	39	8	9	9	10	11
Tb	3.2	4.0	2.9	4.2	2.7	2.6	5.3	1.1	1.1	1.2	1.3	1.5
Dy	18	24	17	24	15	14	28	6	6	7	7	8
Ho	3.5	5.1	3.3	4.5	2.7	2.6	4.6	1.0	1.0	1.1	1.2	1.4
Er	9.7	14.3	9.1	12.2	7.4	7.0	11.5	2.9	2.7	3.0	3.1	3.6
Tm	1.4	2.0	1.4	1.7	1.0	1.0	1.5	0.4	0.4	0.4	0.4	0.5
Yb	8.7	12.4	8.6	10.2	5.9	6.0	8.5	2.4	2.2	2.3	2.6	3.0

(*continued on next page*)

Table A (*continued*)

Profile	Fataga				El Queso			Culata				
Lithology	trachy-phonolite				trachy-rhyolite			trachyte				
Lu	1.2	1.8	1.2	1.4	0.9	0.8	1.1	0.3	0.3	0.3	0.4	0.4
ΣREE	1036	1171	994	1139	588	601	1584	449	471	498	436	448
REE vs.R (%)	–	13	-4	10	–	2	169	–	5	11	-3	0
Ce/Ce*	1.0	1.3	1.3	0.9	1.0	1.1	0.9	1.0	1.0	0.9	1.3	1.0
Eu/Eu*	0.8	0.8	0.8	0.9	0.9	0.9	1.0	1.1	1.1	1.0	1.0	1.0
LREE/HREE	22	17	22	19	16	17	25	31	33	33	26	23
V-index	1.1	1.9	2.1	1.8	0.4	1.3	1.3	1.7	1.7	1.8	2.3	2.1
CIA-index	46	56	73	70	48	53	45	52	53	54	66	63

Oxides formulae and LOI values are shown in wt% (1 wt% equals 10,000 mg kg-1), and the REE in mg kg^{-1}. REE vs.R (%) is the REE concentrarion in the bedrock (R), in percentage. Ce/Ce* = CeN/(LaN x PrN)$^{0.5}$; Eu/Eu* = EuN/(SmN x GdN)$^{0.5}$; V index (Vogt's Residual Index) = (Al2O3 + K2O)/(MgO + CaO + Na2O). CIA index (Chemical Index of Alteration) = 100*(Al_2O_3)/(Al_2O_3 + K_2O + CaO + Na_2O).

Table B

Minor and trace element geochemistry of samples from the selected weathering profiles (all values in mg kg^{-1}, except Au in ppb). Geochemical composition of the samples from the studied weathering profiles.

Profile	Fataga				El Queso			Culata				
Lithology	trachy-phonolite				trachy-rhyolite			trachyte				
Sample	REE-01	REE-02	REE-03	REE-04	REE-13	REE-14	REE-16	REE-18	REE-19	REE-21	REE-22	REE-23
Horizon	R-PH	C-PH	B-PH	B′-PH	R-RH	C-RH	B-RH	R-TR	C2-TR	C1-TR	B-TR	BA-TR
Ag	3.1	4.6	3.8	2.9	2.1	1.8	< 0.5	1.6	1.2	1.4	2.3	
As	16	15	< 5	< 5	7	5	4	< 1	1	2	5	< 5
Au	< 1	2	< 1	< 1	7	< 1	< 1	< 1	3	< 1	< 1	< 1
Ba	23	23	98	116	616	608	300	1690	1612	1702	1000	1123
Be	12	15	24	13	5	8	16	4	4	4	4	4
Bi	< 0.1	0.1	< 0.4	< 0.4	< 0.1	< 0.1	0.3	< 0.1	< 0.1	< 0.1	< 0.4	< 0.4
Br	7.0	< 0.5	< 0.5	2.1	< 0.5	2.1	< 0.5	< 0.5	< 0.5	< 0.5	< 0.5	< 0.5
Cd	< 0.5	< 0.5	< 0.5	< 0.5	< 0.5	< 0.5	< 0.5	< 0.5	< 0.5	< 0.5	< 0.5	< 0.5
Co	< 0.1	< 0.1	2.0	4.0	< 0.1	6.6	70.2	9.8	6.6	10.6	12	22
Cr	31	23	30	40	12	29	1160	28	45	29	130	130
Cs	2.6	1.1	3.0	2.3	0.1	2.2	4.4	0.3	0.4	0.9	0.9	1.2
Cu	3	2	10	10	2	13	96	12	10	9	40	80
Ga	39	42	37	31	32	32	20	28	29	28	28	27
Ge	2	2	2	1	2	2	1	1	1	1	1	1
Hf	1.2	1.8	23.6	18.4	0.9	0.8	6.6	0.3	0.3	0.3	14.2	13.0
Ho	3.5	5.1	3.3	4.5	2.7	2.6	4.6	1.0	1.0	1.1	1.2	1.4
In	0.2	0.2	0.2	0.2	0.1	0.1	0.1	< 0.1	< 0.1	< 0.1	< 0.2	< 0.2
Mo	4	< 2	< 2	< 2	< 2	4	< 2	< 2	< 2	< 2	< 2	2
Nb	410	416	269	267	121	151	295	119	136	129	122	124
Ni	11	7	< 20	< 20	3	14	763	21	15	17	40	50
Pb	15	15	21	21	6	8	38	< 5	< 5	5	8	8
Rb	122	105	69	68	80	81	22	76	80	72	54	68
S	32	8	n.d.	n.d.	59	39	9	6	5	4	n.d.	n.d.
Sb	0.7	0.2	0.5	< 0.5	0.4	0.9	1.8	0.2	0.2	0.2	< 0.5	< 0.5
Sc	3	3	4	6	8	8	28	4	4	4	13	13
Se	< 0.5	5.8	< 0.5	< 0.5	< 0.5	4.3	< 0.5	< 0.5	< 0.5	< 0.5	n.d.	n.d.
Sn	7	7	5	5	6	6	4	2	2	2	2	2
Sr	71	67	104	98	26	418	410	1464	1483	1472	869	928
Ta	24	26	17	16	9	9	4	7	7	7	7	7
Th	27	31	21	20	12	13	61	12	12	12	13	12
Tl	0.2	0.1	0.2	0.2	< 0.1	0.1	0.1	0.1	0.1	0.1	< 0.1	< 0.1
U	7	4	6	7	2	4	6	3	3	3	4	4
V	51	42	36	43	16	58	221	127	121	121	253	254
W	< 1	< 1	2	2	< 1	< 1	< 1	< 1	< 1	< 1	2	2
Y	102	158	82	123	74	73	121	29	29	30	31	39
Zn	319	295	290	330	169	256	270	121	104	117	60	90
Zr	1555	1676	1213	966	991	1124	330	739	749	757	769	725

Table C
The change of percentage ratio values (Eq. (1)) from B and C horizons with regards to the bedrock of the major and trace elements, including the ΣREE. These values are also shown as graphs in Figs. 11 and 12. The elements and oxides are ordered as in Figs. 11 and 12.

From Fig. 10	C-PH	B-PH	C-RH	BC-RH	C-TR	B-TR
MgO	5	−95	178	1131	−21	30
CaO	−25	−49	413	710	−15	−43
P_2O_5	−43	−99	513	499	−17	−21
Fe_2O_3	7	−88	42	273	−13	61
TiO_2	5	−94	68	261	−3	60
ΣREE	13	10	2	169	6	−3
MnO	−10	−100	−9	−8	−25	−38
Al_2O_3	6	−96	23	−22	0	−2
SiO_2	−3	−17	−14	−34	2	−15
Na_2O	−41	−94	−41	−75	3	−48
K_2O	−3	−26	−28	−84	−7	−39
From Fig. 11	C-PH	B-PH	C-RH	BC-RH	C-TR	B-TR
Cr	−25	3	153	9987	−71	−79
Cu	−80	−70	550	4700	−76	−70
Cs	−63	−13	2100	4300	−28	−67
Sr	−36	−32	1508	1477	70	68
Hf	2490	2195	5	−68	3900	3597
V	17	42	263	1281	−52	−50
Pb	−29	−29	33	533	−38	−50
Th	47	32	5	395	−5	−5
Sb	−60	40	125	350	0	0
Sc	−30	−32	3	267	−67	−68
Be	−38	−50	60	220	0	0
U	−26	22	74	169	−8	−8
Nb	55	52	25	144	9	−2
Y	93	24	−1	64	−5	−6
Zn	2	10	51	60	84	102
Sn	40	40	0	−33	0	0
Ge	5	−20	13	−38	−20	−20
Ga	14	5	0	−38	2	0
Ba	−77	−77	−1	−51	66	69
Ta	54	42	0	−60	2	−3
Zr	38	28	13	−67	−2	−4
Rb	52	77	1	−73	41	41
Ag	21	−18	−14	−81	−43	−30

Table D
The change of percentage ratio values (Eq. (1)) from B and C horizons with regards to the REE in the bedrock. These values are also shown as graphs in Fig. 13. The elements and oxides are ordered as in Fig. 13.

From Fig. 12	C-PH	B-PH	B′-PH	C-RH	BC-RH	C2-TR	C1-TR	B-TR	BA-TR
La	−1	4	−17	−1	245	5	15	−22	−10
Ce	25	1	7	6	167	5	7	4	−4
Pr	−7	15	−17	0	160	5	15	−9	0
Nd	−2	31	−10	0	145	3	13	−2	9
Sm	3	37	−6	−4	122	4	12	14	24
Eu	12	58	2	−2	143	6	11	10	25
Gd	22	34	−3	−1	120	5	16	20	41
Tb	27	33	−8	−3	100	4	11	19	38
Dy	33	29	−7	−5	89	5	12	21	40
Ho	47	30	−4	−3	71	0	7	15	35
Er	47	26	−6	−5	56	−5	4	9	26
Tm	39	21	−5	−4	54	−6	0	11	26
Yb	42	17	−2	1	44	−7	−5	7	24
Lu	43	11	2	−3	28	−3	−2	6	21

References

Aiglsperger, T., Proenza, J.A., Lewis, J.F., Labrador, M., Svojtka, M., Rojas-Purón, A., Longo, F., Durisová, J., 2016. Critical metals (REE, Sc, PGE) in Ni laterites from Cuba and the Dominican Republic. Ore Geol. Rev. 73, 127–147.

Angelica, R.S., da Costa, M.L., 1991. Geochemistry of rare-earth elements in surface lateritic rocks and soils from the Maicuru Complex, Para, Brazil. J. Geochem. Explor. 47, 165–182.

Balcells, R., Barrera, J.L., Gómez, J.A., Cueto, L.A., 1992. Mapa Geológico de España escala 1:100.000 1ª edición (MAGNA). Hoja de la Isla de Gran Canaria (21–21/21–22). Instituto Tecnológico Geominero de España (ITGE). Serv. Pub. M° Industria, Madrid.

Bao, Z., Zhao, Z., 2008. Geochemistry of mineralization with exchangeable REY in the weathering crusts of granitic rocks in South China. Ore Geol. Rev. 33, 519–535.

Bellido-Mulas, F., Pineda-Velasco, A., 2008. Mapa Geológico Digital continuo E. 1: 25.000, Zona Canarias - Gran Canaria. (Zona-2912). In: GEODE. Mapa Geológico Digital continuo de España, [Online]. Available: http://info.igme.es/cartografiadigital/geologica/geodezona.aspx?id=z2912, Accessed date: 1 March 2018.

Benaouda, R., Devey, C.W., Badra, L., Ennaciri, A., 2017. Light rare-earth element mineralization in hydrothermal veins related to the Jbel Boho alkaline igneous complex, AntiAtlas/Morocco: the role of fluid-carbonate interactions in the deposition of synchysite-(Ce). J. Geochem. Explor. 177, 28–44.

Bern, C.R., Yesavagea, T., Foley, N.K., 2017. Ion-adsorption REEs in regolith of the Liberty Hill pluton, South Carolina, USA: an effect of hydrothermal alteration. J. Geochem.

Explor. 172, 29–40. https://doi.org/10.1016/j.gexplo.2016.09.009.
Beyala, V.K.K., Onanab, V.L., Prisoa, E.N.E., Parisotc, J.-C., Ekodeck, G.E., 2009. Behaviour of REE and mass balance calculations in a lateritic profile over chlorite schists in South Cameroon. Chem. Geol. 363, 56–75.
Bockheim, J.G., Gennadiyev, A.N., 2000. The role of soil-forming processes in the definition of taxa in Soil Taxonomy and the World Soil Reference Base. Geoderma 95 (1–2), 53–72.
Braun, J.-J., Pagel, M., Herbillon, A., Rosin, C., 1993. Mobilization and redistribution of REEs and Thorium in a syenitic lateritic profile—a mass-balance study. Geochim. Cosmochim. Acta 57 (18), 4419–4434.
Braun, J.-J., Viers, J., Dupre, B., Polve, M., Ndam, J., Muller, J.-P., 1998. Solid/liquid REE fractionation in the lateritic system of Goyoum, East Cameroon: the implication for the present dynamics of the soil covers of the humid tropical regions. Geochim. Cosmochim. Acta 62 (2), 273–299.
Brimhall, G.H., Dietrich, W.E., 1987. Constitutive mass balance relations between chemical composition, volume, density, porosity, and strain in metasomatic hydrochemical systems: results on weathering and pedogenesis. Geochim. Cosmochim. Acta 51, 567–587.
Brioschi, L., Steinmann, M., Lucot, E., Pierret, M.C., Stille, P., Prunier, J., Badot, P.M., 2013. Transfer of rare earth elements (REE) from natural soil to plant systems: implications for the environmental availability of anthropogenic REE. Plant Soil 366, 143–163.
Calagari, A.A., Kangarani Farahani, F., Abedini, A., 2015. Geochemical characteristics of a laterite: the Jurassic Zan Deposit, Iran. Acta Geodyn. Geomater. 12 (1–177), 67–77.
Caroff, M., Maury, R.C., Vidal, Ph., Guille, G., Dupuy, C., Cotten, J., Guillou, H., Gillot, P.-Y., 1995. Rapid temporal changes in Ocean Island Basalt composition: evidence from a 800 m deep drill hole in Eiao shield (Marquesas). J. Petrol. 36, 1333–1365.
Carracedo, J.C., Pérez-Torrado, F.J., Ancochea, E., Meco, J., Hernán, F., Cubas, C.R., Casillas, R., Rodríguez-Badiola, E., Ahijado, A., 2002. Cenozoic volcanism II, the Canary Islands. In: Gibsson, W., Moreno, T. (Eds.), The Geology of Spain. The Geological Society, London (UK), pp. 439–472.
Chai, D.H., Qu, Z.M., Chen, H.C., Chai, F., 2001. New discovery and industrial significance of rare and rare-earth elements in Shanxi bauxite. Light Metals 6, 6–11.
Chang, C., Li, F., Liu, C., Gao, J., Tong, H., Chen, M., 2016. Fractionation characteristics of rare earth elements (REEs) linked with secondary Fe, Mn, and Al minerals in soils. Acta Geochim 35 (4), 329–339. https://doi.org/10.1007/s11631-016-0119-1.
Compton, J.S., White, R.A., Smith, M., 2003. Rare earth element behavior in soils and salt pan sediments of a semi-arid granitic terrain in the Western Cape, South Africa. Chem. Geol. 201, 239–255.
Condie, K.C., Dengate, J., Cullers, R.L., 1995. Behavior of rare earth elements in a paleoweathering profile on granodiorite in the Front Range, Colorado, USA. Geochim. Cosmochim. Acta 59, 279–294.
Connelly, N.G., Damhus, T., Harsthorn, R.M., Hutton, A.T., 2005. Nomenclature of Inorganic Chemistry: Iupac Recommendations. International Union of Pure an Applied Chemistry, Cambridge.
Coppin, F., Berger, G., Bauer, A., Castet, S., Loubet, M., 2002. Sorption of lanthanides on smectite and kaolinite. Chem. Geol. 182, 57–68.
Cornell, R.M., Schwertmann, U., 2003. The Iron Oxides: Structure, Properties, Reactions, Occurrences and Uses. vol. 2003. Wiley–VCH, Weinheim, pp. 439–452.
Deady, E.A., Mouchos, E., Goodenough, K., Williamson, B.J., Wall, F., 2016. A review of the potential of rare-earth element resources from European red muds: examples from Seydisehir, Turkey and Parnassus-Giona, Greece. Mineral. Mag. 80, 43–61.
Dill, H.G., Fricke, A., Henning, K.-H., 1995. The origin of Ba and REE-bearing aluminium-phosphate–sulphate minerals from the Lohrheim kaolinitic clay deposit (Rheinisches Schiefergebirge, Germany). Appl. Clay Sci. 10, 231–245.
Duddy, I.R., 1980. Redistribution and fractionation of rare earth and other elements in a weathering profile. Chem. Geol. 30, 363–381.
Eliopoulos, D., Economou, G., Tzifas, I., Papatrechas, C., 2014. The potential of rare Earth elements in Greece. In: European Rare Earth Resources Conference, Proceedings, pp. 308–316.
European Commission, 2014. Report on Critical Raw Materials or the EU; Report of the Ad Hoc Working Group on Defining Critical Raw Materials. http://ec.europa.eu/DocsRoom/documents/10010/attachments/1/translations/en/renditions/native.
Feng, M.-H., Ngwenya, B.T., Wang, L., Li, W., Olive, V., Ellam, R.M., 2011. Bacterial dissolution of fluorapatite as a possible source of elevated dissolved phosphate in the environment. Geochim. Cosmochim. Acta 75, 5785–5796.
Feraud, G., Schmincke, H.U., Lietz, J., Gastaud, J., Pritchard, G., Bleil, U., 1981. New K7ar ages, chemical analyses and magnetic data of rocks from the islands of Santa Maria (Azores), Porto Santo and Madeira (Madeira archipelago) and Gran Canaria (Canary Islands). Bull. Volcanol. 44, 359–375.
Fernández-Caliani, J.C., 2018. Rare-earth element and stable isotope signatures of kaolin from a Pliocene lateritic weathering profile at mid-latitude region (Andalusia, Spain): Implications for paleoweathering and paleoclimatic reconstructions. Catena 167, 160–170.
Fernandez-Caldas, F., Tejedor, M.L., Quantin, P., 1982. Suelos de regiones volcánicas. Tenerife. Colección Viera y Clavijo IV, Santa Cruz de Tenerife. pp. 250.
Foley, N., Ayuso, R.A., 2013. Rare earth element mobility in high-alumina altered metavolcanic deposits, South Carolina, USA. J. Geochem. Explor. 133, 50–67.
Foley, N., Ayuso, R., 2015. REE enrichment in granite-derived regolith deposits of the Southeastern United States: prospective source rocks and accumulation processes. In: Simandl, G.J., Neetz, M. (Eds.), Symposium on Strategic and Critical Materials Proceedings, November 13–14, 2015, Victoria, British Columbia, British Columbia Ministry of Energy and Mines, British Columbia Geological Survey Paper 2015–3, pp. 131–138.
Freundt, A., Schmincke, H.U., 1995. Eruption and emplacement of a basaltic welded ignimbrite during caldera formation on Gran Canaria. Bull. Volcanol. 56, 640–659.
Fuster, J.M., Hernández Pacheco, A., Muñoz, M., Rodríguez Badiola, E., García Cacho, L., 1968. Geology and vulcanology of the Canary Islands, Gran Canaria. In: Instituto Lucas Mallada (CSIC), Madrid, International Symposium on Volcanlogy, Tenerife, Sept. 1968. Spec. Pub, (243 pp).
Galán, E., Fernández-Caliani, J.C., Miras, A., Aparicio, P., Márquez, M.G., 2007. Residence and fractionation of rare earth elements during kaolinization of alkaline peraluminous granites in NW Spain. Clay Miner. 42, 341–352.
Gálvez, N., Barrón, V., Torrent, J., 1999. Preparation and properties of hematite with structural phosphorus. Clays & Clay Min 47, 375–385.
Gambogi, J., 2017. Rare Earths. U.S. Geological Survey. In: Mineral Commodity Summaries, pp. 134–135.
Guillou, H., Pérez-Torrado, F.J., Hansen-Machin, A.R., Carracedo, J.C., Gimeno, D., 2004. The Plio-Quaternary volcanic evolution of Gran Canaria based on new K-Ar ages and magnetostratigraphy. J. Volcanol. Geotherm. Res. 135, 221–246.
Harlavan, Y., Erel, Y., 2002. The release of Pb and REE from granitoids by the dissolution of accessory phases. Geochim. Cosmochim. Acta 66, 837–848.
Hekinian, R., Stoffers, P., Cheminée, J.L., 2004. Oceanic Hotspots. Intraplate Submarine Magmatism and Tectonism. Springer, pp. 479.
Henderson, P., 1984. General geochemical properties and abundances of the rare earth elements. In: Henderson, P. (Ed.), Rare Earth Element Geochemistry: Developments in Geochemistry. vol. 2 Elsevier Science Publishers, Amsterdam.
Hollik, J.S., Rabinowitz, P.D., Austin, J.A., 1991. Effects of Canary hotspot volcanism on the structure of oceanic crust off Morocco. J. Geophys. Res. 96 (B7), 12039–12067.
Instituto Canario de Estadística, ISTAC, 2017. Canarias en Cifras. Available from: http://www.gobiernodecanarias.org/istac/temas_estadisticos/sintesis/operacion_C00053A.html.
Irvine, T.N., Baragar, W.R.A., 1971. A guide to the chemical classification of the common volcanic rocks. Can. J. Earth Sci. 8 (5), 523–548. https://doi.org/10.1139/e71-055.
Janots, E., Negro, F., Brunet, F., Goffé, B., Engi, M., 2006. Evolution of the REE mineralogy in HP–LT metapelites of the Sebtide complex, Rif, Morocco: Monazite stability and geochronology. Lithos 87, 214–234.
Jowitt, S.M., Medlin, C.C., Cas, R.A.F., 2017. The rare earth element (REE) mineralisation potential of highly fractionated rhyolites: a potential low-grade, bulk tonnage source of critical metals. Ore Geol. Rev. 86, 548–562.
Karakaya, N., 2009. REE and HFS element behaviour in the alteration facies of the Erenler Dağı Volcanics (Konya, Turkey) and kaolinite occurrence. J. Geochem. Explor. 101, 185–208.
Laveuf, C., Cornu, S., 2009. A review on the potentiality of Rare Earth Elements to trace pedogenetic processes. Geoderma 154, 1–12.
Le Bas, M.J., Le Maitre, R.W., Streckeisen, A., Zanettin, B., 1986. A chemical classification of volcanic rocks based on the total alkali-silica diagram. J. Petrol. 27 (3), 745–750. https://doi.org/10.1093/petrology/27.3.745.
Le Dez, A., Maury, R.C., Vidal, P., Bellon, H., Cotten, L., Brousse, R., 1996. Geology and geochemistry of Nuku Hiva, Marquesas: temporal trends in a large Polynesian shield volcano. Bull. Soc. Geol. France 167, 197–209.
Li, H.J., Wang, Q.C., Li, Z., 2005. Characteristics of Mesozoic and Cenozoic heavy minerals from Kuche River section in Kuche depression and their geological implications. Acta Petrol. Mineral. 24 (1), 53–61.
Lietz, J., Schmincke, H.U., 1975. Miocene–Pliocene sea-level changes and volcanic phases on Gran Canaria (Canary Islands) in the light of new K/Ar-ages. Palaeogeography Palaeoclimatology and Palaeoclimatology 18, 213–239.
Long, K.R., Van Gosen, B.S., Foley, N.K., Cordier, D., 2010. The Principal Rare Earth Elements Deposits of the United States — A Summary of Domestic Deposits and a Global Perspective – U.S. Geological Survey Scientific Investigations Report 2010–5220, Reston, VA, USA. pp. 1–104.
Ma, J., Wei, G., Xu, Y., Long, W., Sun, W., 2007. Mobilization and re-distribution of major and trace elements during extreme weathering of basalt in Hainan Island. South China. Geochim. Cosmochim. Acta 71, 3223–3237.
MacKenzie, W.S., Donalson, C.H., Guildford, C., 1984. Atlas of Igneous Rocks and their Textures. Logman, London (148pp.).
Marques, J.J., Schulzeb, D.G., Curia, N., Mertzman, S.A., 2004. Trace element geochemistry in Brazilian Cerrado soils. Geoderma 121, 31–43.
McDonough, W.F., Sun, S., 1995. The composition of the Earth. Chem. Geol. 120, 223–253.
McDougall, I., Schmincke, H.U., 1976. Geochronology of Gran Canaria, Canary Islands: age of shield building volcanism and other magmatic phases. Bull. Volcanol. 40, 1–21.
McLennan, S.M., Hemming, S., McDaniel, D.K., Hanson, G.N., 1993. Geochemical approaches to sedimentation, provenance, and tectonics. In: Johnsson, M.J., Basu, A. (Eds.), Processes Controlling the Composition of Clastic Sediments. Geol. Soc. Am. Spec. Pap. 284. pp. 21–40.
Mehra, O.P., Jackson, M.L., 1960. Iron oxide removal from soils and clays by a dithionite-citrate system buffered with sodium bicarbonate. Clay Clay Miner. 7 (1), 317–327.
Menéndez, I., Díaz-Hernandez, J.L., Mangas, J., Alonso, I., Sánchez-Soto, P.J., 2007. Airborne dust accumulation and soil development in the north-east sector of Gran Canaria (Canary Island, Spain). Journal of Arid Environment 71, 57–81.
Menéndez, I., Mangas, J., Tauler, E., Barrón, V., Torrent, J., Betancort, J.F., Santana, A., Recio, J.M., Quevedo-González, L.A., Alonso, I., Méndez, J., 2019. Aeolian influx and related environmental conditions on Gran Canaria during the early Pleistocene – ERRATUM. Quaternary Research, 91(1), 452-452. doi:10.1017/qua.2019.3 Aeolian influx and related environmental conditions on Gran Canaria during the early Pleistocene. Quat. Res. 91 (1), 35–50. https://doi.org/10.1017/qua.2018.64.
Mizota, C., Matsuhisa, Y., 1995. Isotopic evidence for the eolian origin of quartz and mica in soils developed on volcanic materials in the Canary Archipelago. Geoderma 66, 313–320.
Mongelli, G., 1993. REE and other trace elements in a granitic weathering profile from

"Serre", southern Italy. Chem. Geol. 103, 17–25.
Mongelli, G., 1997. Ce-anomalies in the textural components of upper Cretaceous karst bauxites from the Apulian carbonate platform (southern Italy). Chem. Geol. 140 (1–2), 69–79.
Nahon, D., Merino, E., 1996. Pseudomorphic replacement versus dilation in laterites: petrographic evidence, mechanisms, and consequences for modelling. J. Geochem. Explor. 57 (1–3), 217–225.
Nesbitt, H.W., 1979. Mobility and fractionation of rare earth elements during weathering of a granodiorite. Nature 279, 206–210.
Nesbitt, H.W., Young, G.M., 1989. Formation and diagenesis of weathering profiles. J. Geol. 97, 129–147.
Oelkers, E.H., Poitrasson, F., 2002. An experimental study of the dissolution stoichiometry and rates of a natural monazite as a function of temperature from 50 to 230 jC and pH from 1.5 to 10. Chem. Geol. 191, 73–87.
Ohta, A., Kawabe, I., 2001. REE(III) adsorption onto Mn dioxide (δ-MnO_2) and Fe oxyhydroxide: Ce(III) oxidation by δ-MnO_2. Geochim. Cosmochim. Acta 65, 695–703.
Panahi, A., Young, G.M., Rainbird, R.H., 2000. Behaviour of major and trace elements (including REE) during Paleoproterozoic pedogenesis and diagenetic alteration of an Archaean granite near Ville Marie, Quebec, Canada. Geochim. Cosmochim. Acta 64 (13), 2199–2220.
Pérez-Torrado, F., Carracedo, J.C., Mangas, J., 1995. Geochronology and stratigraphy of the Roque Nublo Group, Gran Canaria, Canary Islands. J. Geol. Soc. Lond. 152, 807–818.
Pokrovsky, O.S., Schott, J., Dupre, B., 2006. Trace element fractionation and transport in boreal rivers and soil pore waters of permafrost-dominated basaltic terrain in Central Siberia. Geochim. Cosmochim. Acta 70 (13), 3239–3260.
Pourret, O., Davranche, M., 2013. Rare earth element sorption onto hydrous manganese oxide: a modelling study. J. Colloid Interface Sci. 395, 18–23.
Price, J.R., Velbel, M.A., 2003. Chemical weathering indices applied to weathering profiles developed on heterogeneous felsic metamorphic parent rocks. Chem. Geol. 202, 397–416.
Reinhardt, N., Proenza, J.A., Villanova-de-Benavent, C., Aiglsperger, T., Bover-Arnal, T., Torró, L., Salas, R., Dziggel, A., 2018. Geochemistry and Mineralogy of Rare Earth Elements (REE) in Bauxitic Ores of the Catalan Coastal Range, NE Spain. Minerals 8, 562.
Rudnick, R.L., Gao, S., 2003. Composition of the continental crust. In: Treatise on Geochemistry. Volume 3. 0-08-044338-9, pp. 1–64.
Sanematsu, K., Kon, Y., Imai, A., 2013. Influence of phosphate on mobility and adsorption of REEs during weathering of granites in Thailand. J. Asian Earth Sci. 111, 14–30.
Santana, I.V., Wall, F., Botelhob, N.F., 2015. Occurrence and behavior of monazite-(Ce) and xenotime-(Y) in detrital and saprolitic environments related to the Serra Dourada granite, Goiás/ Tocantins State, Brazil: potential for REE deposits. J. Geochem. Explor. 155, 1–13.
Scheinost, A.C., Chavernas, A., Barron, V., Torrent, J., 1998. Use and limitations of second derivative diffuse reflectance spectroscopy in the visible to near-infrared range to identify and quantity Fe oxide minerals in soils. Clay Clay Miner. 46, 528–536.
Schmincke, H.U., Sumita, M., 2010. Geological Evolution of the Canary Islands: A Young Volcanic Archipelago Adjacent to the Old African Continent. Ed. Görres, Koblenz. (200 pp).
Schirnick, C., van den Bogaard, P., Schmincke, H.U., 1999. The Miocene Tejeda complex on Gran Canaria (Canary Islands)-Cone sheet formation and intrusive growth of an oceanic island. Geology 27, 207–210.
Schmincke, H.U., 1976. The geology of the Canary Islands. In: Kunkel, G. (Ed.), Biogeografphy and Ecology in the Canary Islands. Junk, The Hague, pp. 67–184.
Schmincke, H.U., 1982. Volcanologic and chemical evolution of the Canary Islands. In: Rad v, U. (Ed.), Geology of the Northwest African Continental Margin. Springer-Verlag, Berlin Heidelberg New York, pp. 273–306.
Schmincke, H.U., 1990. Geological field guide of Gran Canaria. In: IAVCEI, Int. Volc. Congr. Mainz, Germany, (227 pp).
Schmincke, H.U., Swanson, D.A., 1966. Eine alte Caldera auf Gran Canaria. N. Jb. Geol. Pal. Mh. 260–269.
Schwertmann, U., 1964. Differenzierung der Eisenoxide des Bodens durch Extraktion mit sauerAmmoniumoxalat-Lösung. Zeitschrift fur Pflanzenernahrung und Bodenkunde 105, 194–202.
Scott, H.M., 1987. Solid solution in, and classification of, gossan-derived members of the alunite-jarosite family, Northwest Queensland, Australia. Am. Miner. 72, 178–l 87.
Staudigel, H., Clague, D.A., 2010. The geological history of deep sea volcanoes. Biosphere, hydrosphere and lithosphere interactions. Oceanography 23, 58–71.
Steiner, C., Hobson, A., Favre, P., Stamply, G.M., 1998. Early Jurassic sea-floor spreading in the central Atlantic-the Jurassic sequence of Fuerteventura (Canary Islands). Geol. Soc. Am. Bull. 110, 1304–1317.
Stoffregen, R.E., Alpers, C.N., 1987. Woodhouseite and svanbergite in hydrothermal ore deposits: product of apatite destruction during advanced agillic alteration. Can. Mineral. 25, 201–211.
Taunton, A.E., Welch, S.A., Banfield, J.F., 2000. Microbial controls on phosphate and lanthanide distributions during granite weathering and soil formation. Chem. Geol. 169 (3–4), 371–382.
Torrent, J., Barrón, V., 2002. Diffuse reflectance spectroscopy of iron oxides. In: Hubbard, A.T. (Ed.), Encyclopedia of Surface and Colloid Science. vol. 1. Marcel Dekker, New York, pp. 1438–1446.
Torrent, J., Liu, Q., Bloemendal, J., Barron, V., 2007. Magnetic enhancement and iron oxides in the upper Luochuan loess-paleosol sequence, Chinese Loess Plateau. Soil Sci. Soc. Am. J. 71, 1570–1578.
Torró, L., Proenza, J.A., Aiglsperger, T., Bover-Arnal, T., Villanova-de-Benavent, C., Rodríguez-García, D., Ramírez, A., Rodríguez, J., Mosquea, L.A., Salas, R., 2017. Geological, geochemical and mineralogical characteristics of REE-bearing Las Mercedes bauxite deposit, Dominican Republic. Ore Geol. Rev. 89, 114–131.
Tripathi, J.K., Rajamani, V., 2007. Geochemistry and origin of ferruginous nodules in weathered granodioritic gneisses, Mysore Plateau, Southern India. Geochim. Cosmochim. Acta 71, 1674–1688.
Tyler, G., 2004. Vertical distribution of major, minor, and rare elements in a Haplic Podzol. Geoderma 119 (3–4), 277–290.
van den Bogaard, P., 2013. The origin of the Canary Island seamounts province: new ages of old seamounts. Sci. Rep. 3–2107.
van den Bogaard, P., Schmincke, H.U., 1998. Chronostratigraphy of Gran Canaria. In: Waver, P.P.E., Schmincke, H.U., Firth, J.V., Fuffield, W.A. (Eds.), Proce. ODP, Sci. Results. vol. 157. Ocean Drilling Program, College Station, TX, pp. 127–140.
Vera, J.A., 2004. Geología de España. Sociedad Geológica de España-Instituto Geológico y Minero Español, Madrid.
Walker, G.P.L., 1990. Geology and volcanology of Hawaiin Islands. Pac. Sci. 44-4, 315–347.
Wang, L., Li, H.M., Yang, J.D., Qiu, L.W., Chai, D.H., 2000. Discovery of palaeo-weathering type rare earth elements deposits in Northern China and its significance. Geol. J. China Univ. 6 (4), 605–607.
Wang, L., Li, H.M., Yang, J.D., Shen, Y.Q., Chai, D.H., Chen, P., Qiu, L.W., Chen, X.M., Zhao, L.X., Zhu, C., Ge, J.J., 2003. Palaeoweathering type rare earth elements deposit in Shanxi determined by solid isotope mass spectrometry. Journal of Chinese Mass Spectrometry Society 24 (3), 394–397.
Wang, L., Liang, T., Ding, S., Zhang, C., Zhang, G., Wang, X., 2004. Biogeochemical cycle and residue of extraneous rare earth elements in agricultural ecosystem. J. Rare Earths 22 (5), 701–706.
Wang, Q., Deng, J., Liu, X., Zhang, Q., Sun, S., Jiang, C., Zhou, F., 2010. Discovery of the REE minerals and its geological significance in the Quyang bauxite deposit, West Guangxi, China. J. Asian Earth Sci. 39, 701–712.
Williams, M.L., Jercinovic, M.J., Harlov, D.E., Budzyn, B., Hetherington, C.J., 2011. Resetting monazite ages during fluid-related alteration. Chem. Geol. 283, 218–225.
Wilson, M., 1989. Igneous Petrogenesis: A Global Tectonic Approach. Unwin Hyman, London (466p).
Wondraczek, L., Tyystjävi, E., Méndez-Ramos, J., Müller, F.A., Zhang, Q., 2015. Shifting the sun: solar spectral conversion and extrinsic sensitization in natural and artificial photosynthesis. Advanced Science 2, 1500218.
Wood, S.A., 1990. The aqueous geochemistry of the rare-earth elements and yttrium. 1. Review of available low-temperature data for inorganic complexes and the inorganic REE speciation of natural waters. Chem. Geol. 82, 159–186.
Yanots, E., Bernier, F., Brunet, F., Muñoz, M., Trcera, N., Berger, A., Lanson, M., 2015. Ce (III) and Ce(IV) (re)distribution and fractionation in a laterite profile from Madagascar: Insights from in situ XANES spectroscopy at the Ce LIII-edge. Geochim. Cosmochim. Acta 153 (2015), 134–148.
Yusoff, Z.M., Ngwenya, B.T., Parsons, I., 2013. Mobility and fractionation of REEs during deep weathering of geochemically contrasting granites in a tropical setting, Malaysia. Chem. Geol. 349–350, 71–86.
Zapata, F., Roy, R.N., 2004. Use of phosphate rocks for sustainable agriculture. In: Fertilizer and Plant Nutrition, Bulletin 13. FAO Land and Water Development Division and the International Atomic Energy Agency, Rome (172 pp).
Zhao, L., Honga, H., Fanga, Q., Yina, K., Wang, C., Li, Z., Torrent, J., Cheng, F., Algeoa, T.J., 2017. Monsoonal climate evolution in southern China since 1.2 Ma: new constraints from Fe-oxide records in red earth sediments from the Shengli section, Chengdu Basin. Paleogeography, Palaeoclimate, Palaeoecology 473, 1–15.